

# Advanced signal processing for enhanced damage detection with piezoelectric wafer active sensors

Lingyu Yu<sup>†</sup> and Victor Giurgiutiu<sup>‡</sup>

*Mechanical Engineering Department, University of South Carolina Columbia, SC 29208, USA*

*(Received December 8, 2004, Accepted April 13, 2005)*

**Abstract.** Advanced signal processing techniques have been long introduced and widely used in structural health monitoring (SHM) and nondestructive evaluation (NDE). In our research, we applied several signal processing approaches for our embedded ultrasonic structural radar (EUSR) system to obtain improved damage detection results. The EUSR algorithm was developed to detect defects within a large area of a thin-plate specimen using a piezoelectric wafer active sensor (PWAS) array. In the EUSR, the discrete wavelet transform (DWT) was first applied for signal de-noising. Secondly, after constructing the EUSR data, the short-time Fourier transform (STFT) and continuous wavelet transform (CWT) were used for the time-frequency analysis. Then the results were compared thereafter. We eventually chose continuous wavelet transform to filter out from the original signal the component with the excitation signal's frequency. Third, cross correlation method and Hilbert transform were applied to A-scan signals to extract the time of flight (TOF) of the wave packets from the crack. Finally, the Hilbert transform was again applied to the EUSR data to extract the envelopes for final inspection result visualization. The EUSR system was implemented in LabVIEW. Several laboratory experiments have been conducted and have verified that, with the advanced signal processing approaches, the EUSR has enhanced damage detection ability.

**Keywords:** signal processing; wavelet transform; short-time Fourier transform; Hilbert transform; cross-correlation; damage detection; phased array; piezoelectric sensor; NDE, SHM.

---

## 1. Introduction

### 1.1. Structural health monitoring with piezoelectric wafer active sensors

Structural health monitoring (SHM) is a method of determining the health of a structure from the readings of a number of permanently-attached sensors that are monitored over time. SHM can be performed in two ways, passive and active. Both approaches aim to perform a diagnosis of the structural safety and health, followed by a prognosis of the remaining life. Passive SHM consists of monitoring a number of parameters (loading stress, environment action, performance indicators, acoustic emission from cracks, etc.) and inferring the state of structural health from a structural model. This method uses passive sensors which only "listen" to the structure but do not interact with it. Therefore, passive SHM does not provide a direct measurement of the damage presence and intensity. In contrast, active SHM

---

<sup>†</sup>PhD Candidate, E-mail: [yu3@engr.sc.edu](mailto:yu3@engr.sc.edu)

<sup>‡</sup>Associate Professor, E-mail: [giurgiut@engr.sc.edu](mailto:giurgiut@engr.sc.edu)

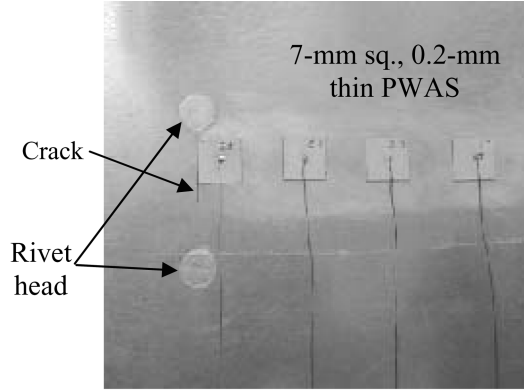


Fig. 1 Piezoelectric wafer active sensors (PWAS) attached to a thin-wall structure

uses active sensors that interact with the structure and thus determine the presence or absence of damage. Active SHM performs proactive interrogation of the structure, detects damage, and determines the state of structural health from the evaluation of damage extent and intensity. The methods used for active SHM, e.g., ultrasonics, eddy currents, etc., resemble those of nondestructive evaluation (NDE), etc., only that they are used with embedded sensors. Hence, the active SHM could be seen as a method of embedded (or in-situ) NDE.

The ultrasonics-based active SHM method uses piezoelectric wafer active sensors (PWAS) to transmit and receive Lamb waves in a thin-wall structure (Fig. 1). PWAS are lighter, smaller, and less expensive than the conventional ultrasonic transducers. PWAS are permanently attached to the structure and permit on-demand structural interrogation. PWAS operate on the piezoelectric principle and achieve direct transduction of electric energy into elastic energy and vice-versa. Their constitutive equations couple the electrical and mechanical variables in the material (mechanical strain,  $S_{ij}$ , mechanical stress,  $T_{kl}$ , electrical field,  $E_k$ , and electrical displacement  $D_j$ ) in the form:

$$\begin{aligned} S_{ij} &= s_{ijkl}^E T_{kl} + d_{kij} E_k \\ D_j &= d_{kij} T_{kl} + \varepsilon_{jk}^T E_k \end{aligned} \quad (1)$$

where  $s_{ijkl}^E$  is the mechanical compliance of the material measured at zero electric field ( $E=0$ ),  $\varepsilon_{jk}^T$  is the dielectric permittivity measured at zero mechanical stress ( $T=0$ ), and  $d_{kij}$  represents the piezoelectric coupling effect. An alternating voltage applied to the PWAS terminals produces an oscillatory expansion and contraction of the PWAS material. Vice-versa, an oscillatory expansion and contraction of the PWAS material produces an alternating voltage at the PWAS terminals. In Lamb-waves applications, PWAS couple their in-plane motion, excited through the piezoelectric effect, with the Lamb-waves particle motion on the material surface.

PWAS bear similarities with conventional ultrasonic transducers because they both use the piezoelectric effect to convert electric signals into acoustic waves (transmission) and acoustic waves back into electric signals (reception). However, PWAS differ from conventional ultrasonic transducers in several ways: (1) PWAS achieve Lamb wave transmission and reception through in-plane strains coupling with the structural surface; (2) PWAS are non-resonant wide-band devices; (3) PWAS are strongly coupled with the Lamb-waves in the structure and can be tuned to excite selective Lamb-wave

modes (Giurgiutiu 2003). The Lamb waves transmitted and received by the PWAS can be used in pitch-catch, pulse-echo, and phased-array methods to detect the presence of cracks, delaminations, disbonds, and corrosion. The Lamb waves travel into the structure and are reflected or diffracted by the structural boundaries, discontinuities, and damage. The reflected or diffracted waves arrive back at the PWAS array where they are transformed into electric signals. Due to the similarities between this approach and NDE ultrasonics, it can be termed embedded ultrasonics. Embedded ultrasonics will allow the transitioning of conventional ultrasonic methods to structural health monitoring (SHM).

Of particular interest is the phased-array implementation of this concept (Giurgiutiu and Bao 2002). A phased-array can be programmed to have different sensitivities to signals from different directions and can be oriented and adjusted such that the direction of interest responds to the greatest sensitivity. The array response is a function of both time and the orientation angle. The angle relative to the greatest array response and the distance to the damage from the array need to be determined. To determine the distance, the time of flight of echoes needs to be detected first (Purekar and Pines 2003, Sundaraman and Adams 2002). A PWAS phased-array can image a wide structural area and detect structural damage using a steering beam of ultrasonic Lamb waves similar to the way phased-array radar uses a steering beam of radio waves. For this reason, Giurgiutiu and Bao (2002) called this embedded ultrasonic structural radar (EUSR). Its implementation is illustrated in Fig. 2a, which shows an aluminum plate instrumented with a number  $M$  of PWAS transducers arranged in a linear phased array. In order to implement the phased array principle, an array of  $M^2$  elemental signals is collected. The elemental signals are obtained by performing excitation of one PWAS and detection on all the PWAS, in a round robin fashion. After the  $M^2$  elemental signals are collected and stored in the computer memory, the phased array principle is applied in virtual time using the EUSR algorithm and the EUSR LabVIEW program. Fig. 2b shows the LabVIEW GUI interface of the EUSR program. The elemental signals are processed using the phased-array beam forming formulas based on the azimuthal angle  $\theta$ . The azimuthal angle  $\theta$  is allowed to vary in the range  $0^\circ$  to  $180^\circ$  to attain, a sweep of the complete half plane. At each azimuthal angle, an A-scan of the Lamb wave beam signal is obtained. If the beam

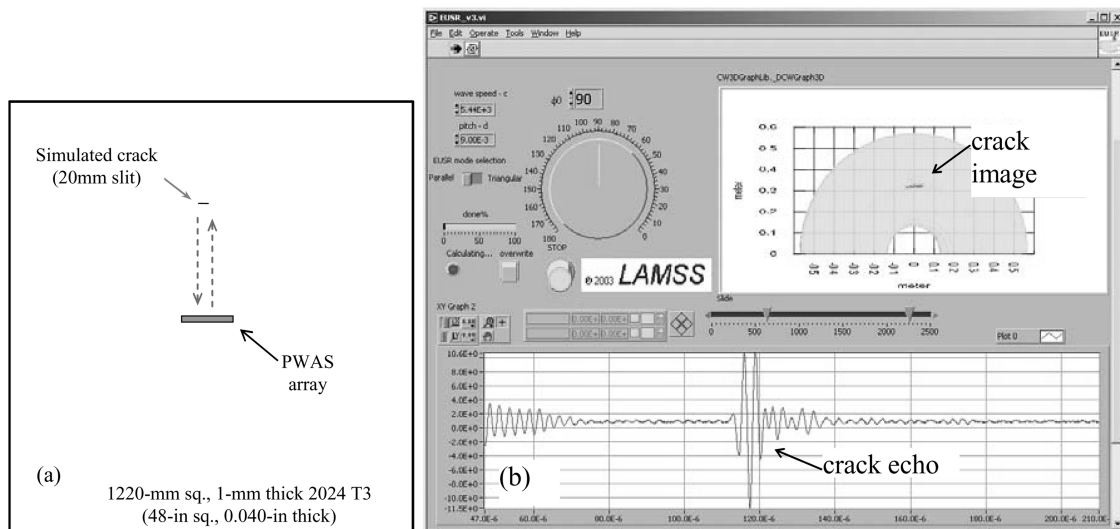


Fig. 2 Crack detection in a square plate with the EUSR method: (a) location and size of simulated broadside crack; (b) imaging and echo of broadside crack in the EUSR algorithm (Giurgiutiu and Bao 2002)

encounters damage, reflection/diffraction from the damage will show as an echo in the A-scan. More details about the EUSR algorithm is provided in the appendix II. In Fig. 2a, the damage is a 20-mm narrow slit simulating a through-the-thickness crack. The A-scan shown in Fig. 2b indicates clearly the crack echo because the scanning beam is oriented at 90°. Azimuthal juxtaposition of all the A-scan signals creates an image of the half plane. The damage is clearly indicated as darker areas. Using the wave speed value, the time domain signals are mapped into the space domain and the geometric position and a measuring grid is superposed on the reconstructed image. Thus, the exact location of the defects can be directly determined.

### 1.2. State of the art in signal processing for active-sensors structural health monitoring

How to identify damage using the information already obtained from structures under inspection is significant to health monitoring and damage detection. Various signal processing methods have been explored and applied for this target. Staszewski (2002) discussed the importance of signal processing for damage detection in composite materials and concluded that many of the recent advances in damage detection can be attributed to the development of advanced signal processing techniques. The major elements of signal processing for damage detection include: data pre-processing, feature extraction and selection, pattern recognition and data/information fusion. For a multi-sensor architecture, it is also important to establish the optimal type, number and location of sensors. It is not only important to obtain features related to damage and to overcome different boundary and environmental conditions, but also to develop automated damage detection system. Kim and Melhem (2004) has done a significant literature review on damage detection of structures by wavelet analysis. Al-khalidy, *et al.* (1997) published numerous papers about damage detection using wavelet analysis. Robertson, *et al.* (1991) presented a wavelet-based method for the extraction of impulse response functions (Markov parameters) from measured input and output data. Kitada (1998) proposed a method of identifying nonlinear structural dynamic systems using wavelets. Other research studies aimed at determining modal parameters using wavelets can be found by Hans, *et al.* (2000), Lamarque, *et al.* (2000) and Ruzzene, *et al.* (1997). Hou, *et al.* (2000) provided numerical simulation data from a simple structural model with breakage springs. Hou and Hera (2001) proposed pseudo-wavelets to identify system parameters, and the associated pseudowavelet transform was developed. Amaravadi, *et al.* (2001) proposed a new technique that combines these two methods for enhancing the sensitivity and accuracy in damage location. Farrar, *et al.* (2001) discussed the construction of integrated structural health monitoring system. One major issue of the implementation of such a system was signal processing to identify damage, which may involve a feature-extraction data compression process, which identifies damage-sensitive properties from the measured vibration response. Al-khalidy, *et al.* (1997) found out that though the most often used signal processing method is the Fourier Transform, its serious drawback is that it loses all the time information so that it is not a proper tool for nonstationary signal analysis. They proposed using short-time Fourier transform (STFT) to correct the deficiency of Fourier transform with windowing technique, by cutting the signal in parts and only analyzing a small section at a time. Since STFT also has the drawback that the size of the time window is the same for all frequencies, Wavelet transform was finally discussed with its ability to detect the trends, breakdown points, discontinuities, and self-similarities, etc. Jiang and Kabeya (1999) proposed another practical and quantitative technique for assessment of the location and characterization of damage using the longitudinal wave propagation measuring method. The pulse-echo method was utilized to send out an interrogation signal and receive the backscatter signals. Hou, *et al.* (2000) emphasized that the signal processing and analysis is a major part of any active SHM system

and presented a novel signal processing method. The signal processing algorithm/software processed the recorded signals and then interpreted them in terms of the physical condition of the structures in order to detect structural damage. Discrete wavelet transform was employed to find out the damage and determine the time of occurrence utilizing the singularity property of wavelet transform. By this means, only a small portion of the data in the vicinity of that moment is involved. The problem with this processing is that it requires a clean environment, no noise disturbance. Mal (2001) proposed an Intelligent Structural Health Monitoring System (ISHMS) for the nondestructive evaluation (NDE) of aircraft and aerospace structures. The signal processing/interpretation methodology consists of signal filtering, and joint time-frequency analysis such as short-time Fourier transform and Wigner-ville distribution, wavelet transforms, and Choi-Williams distribution. Acellent Technologies, Inc. (2003) released the Acellent Software Suite (ACCESS), version 1.0.1, a software solution which allows to select sensors from an internal library, build new sensors, select signal parameters, collect sensor data, export sensor data and integrate application modules for signal processing and data visualization. At this time, ACCESS is developing to have its first application module "hot-spot" imaging for damage detection. Wimmer and DeGiorgi (2004) presented a method using a wavelet based algorithm to interpret the raw data in terms of presence and location of damage to evaluate plate and beam structure's performance. This wavelet based algorithm makes use of the continuous wavelet transform and examines how this feature changes as damage accumulates. Yang, *et al.* (2004) proposed an adaptive tracking technique based on the extended Kalman filter approach to identify the structural parameters and their changes for vibration on-line health monitoring. It is capable of tracking the abrupt change of system parameters from which the event and severity of structural damage can be detected. The proposed adaptive filtering technique is to determine the parametric variation so that the residual error of the estimated parameters is contributed only by the noises of the measured data.

Hilbert transform has been widely used in analytical signal analysis. Hu, *et al.* (2001) used Hilbert transform to pick up the envelopes of vibration signals and then applied wavelet transform to detect the signal singularity for high voltage breaker failure diagnosis. Kang, *et al.* (2000) used Hilbert transform to detect the deflection shapes at one single frequency. They pointed out that compared with other methods like demodulation and Fourier Transform, Hilbert transform is a simple technique and can overcome demodulation and Fourier related problems. Schlaikjer, *et al.* (2003) studied different envelope detector algorithms of the RF-signals which have a limited bandwidth and zero mean. They concluded that in theory Hilbert transform gives the ideal envelope extraction for narrowband signals with no DC component. The cross-correlation method (Knapp and Carter 1976), is one of the most popular technique for time delay estimation by determining the similarity between two objects. Marioli, *et al.* (2000) presented a time of flight determination method based on the use of cross correlation. Both the transmitted signals and echoes were digitized and their cross-correlation coefficients were computed. The time index of the peak of the correlation function measures the delay between the two signals, i.e., the time of flight is determined. Hueber, *et al.* (2000) discussed how to detect the echo delay (time of flight) in an airborne ultrasonic distance measurement system with cross correlation technique, followed by a Hilbert transform based calculation to extract the correlation envelope. Then the position of the peak in the cross correlation function corresponding to the roundtrip time of an acoustic wave then is detected. Normalized cross correlation based method has been used extensively in machine vision for industrial inspection. It is an easy way to evaluate the degree of similarity between two compared images (Tsai, *et al.* 2003). Handzel, *et al.* (2003) described a sound source localizing system which can calculate the source direction using the standard cross-correlation algorithm based on time of arrival of the signals. Du, *et al.* (2004) used cross-correlation to improve earthquake relocation results by selecting those time delays with associated cross correlation coefficients larger than a chosen threshold. The cross

correlation time delays verified with the biospectrum method provided improved (smaller root mean square residual and more clustered) earthquake relocation results.

### *1.3. Research objective*

The objective of our research was to apply advanced signal processing methods to improve the detection capabilities of the EUSR method. In applying signal processing to the PWAS signals we have pursued three main objectives:

1. Signal de-noising
2. Time-frequency analysis of the signal
3. Time-of-flight extraction

In pursuing these objectives, we have considered the following signal processing methods:

1. Digital filters
2. Short time Fourier transform
3. Wavelet transform (discrete and continuous)
4. Hilbert transform
5. Correlation analysis

The application is done on actual signals measured in the Laboratory for Active Materials and Smart Structures in the University of South Carolina using multiple EUSR experiments. Results of the implementation are presented in this paper. In addition, mathematical background of the signal processing methods is offered as appendix I to this paper.

## **2. The experimentation**

A proof-of-concept system has been built in LAMSS to evaluate the feasibility and capability of the EUSR. A 1.6-mm thick, 2024-aluminum alloy rectangular plate (914-mm×504-mm×1.6-mm) was instrumented with a PWAS phased array. The PWAS phased array consists of eight 0.2-mm thick and 7-mm square piezoelectric wafers (American Piezo Ceramics Inc., APC-850). The PWAS free electrical capacitance was 3.3 nF for these 7-mm round. The PWAS were bonded with M-Bond 200 adhesive. The bonding procedure followed Vishay Micro-Measurements Instruction Bulletin B-127-14 for strain gauge installation (Vishay Micro-measurement 2004). The sensors were connected with thin insulated wires AWG 38 with diameter of 0.1 mm to an 8-channel signal bus and an 8-pin connector. An HP33120A signal generator was used to generate Hanning-windowed tone-burst excitation of 10-V amplitude of various frequencies and 10 Hz repetition rate. A Tektronix TDS210 two-channel digital oscilloscope, synchronized with the signal generator, was used to collect the response signals. One of the oscilloscope channels collected the signal from the transmitter PWAS, while the other channel was switched among the remaining PWAS. See Fig. 3a. We have designed several specimens with different crack layout. The size of the simulated cracks is 19-mm (0.750-in) long, 0.127-mm (0.005-in) wide. Fig. 3b shows the setup of the experiment.

The HP33120A was used to generate a 343 kHz Hanning windowed tone-burst excitation with a 10 Hz repetition rate. The Tektronix TDS210 digital oscilloscope, synchronized with the digital generator, was used to collect the response signals from the PWAS array. One of the oscilloscope channels was switched among the remaining elements in the PWAS array by the digitally controlled auto-switching unit.

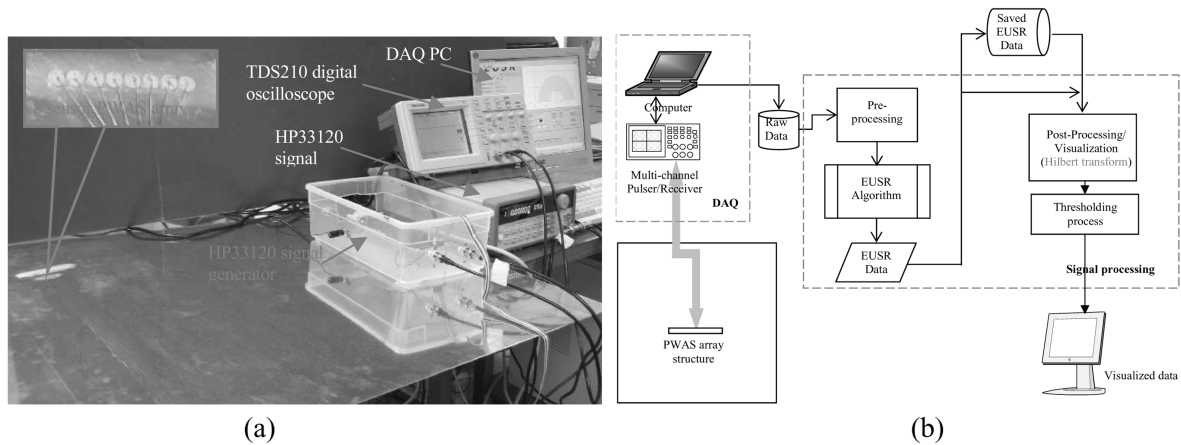


Fig. 3 EUSR experimentation: (a) EUSR experiment setup; (b) EUSR LabVIEW program flowchart

A LabVIEW program was developed to process the collected raw data files. After EUSR algorithm, the resulting data is saved in a EUSR data file on the computer for later retrieval. It also enables other programs to access the EUSR data. Based on the EUSR algorithm, the resulting data file is a collection of signals that represent the structure response at different angles, defined by  $\phi$ , from  $0^\circ$  to  $180^\circ$ . With advanced signal processing techniques, these data was transformed to a 2-D plane domain. A 3-D surface image is generated to represent the intensity of the reflections in the end.

### 3. De-noising by digital filtering and discrete wavelet transform

One serious concern in signal analysis is noise, i. e., how to extract damage information in the presence of noise. Noise is unavoidable. It comes from measurements and also from the signal processing. The noise showing in our experiment was of high frequency. This may affect the detection of high frequency components related to damage. Hence, it is necessary to include a de-noising process to improve the signal analysis. In our research, we comparatively studied de-noising using the digital filtering and DWT de-noising.

#### 3.1. Digital filter de-noising

In our de-noising process, we applied a lowpass filter to remove the high frequency noise using a Chebyshev II, considering it has monotone behavior in the low pass band and relatively short transition band. Other parameters were also adjusted for optimization, such as the filtering mode, cutoff frequency, and filter order. Fig. 4 shows the result obtained by using the Chebyshev type II bandpass filter with order 6 and cutoff frequencies between 3 and 8 MHz.

We see the filtered signal has big deviation from the real signal. Part of the signal centered at the mid was lost while big disturbance presented as side lobes. Though digital filtering is relatively easier to implement, we need to have a new method for de-noising.

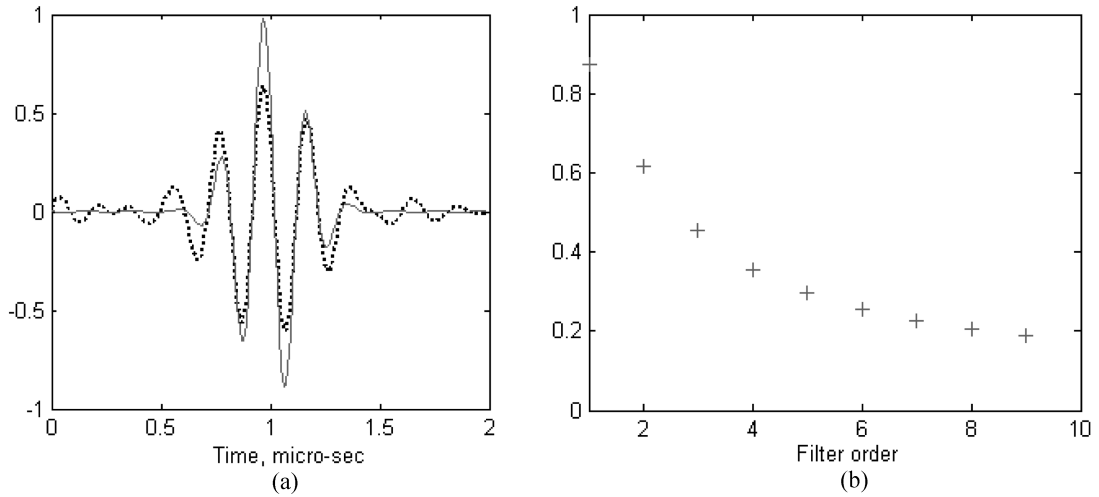


Fig. 4 De-noising with filtering: (a) ideal signal (solid line) and filtered signal (crosses +); (b) error index

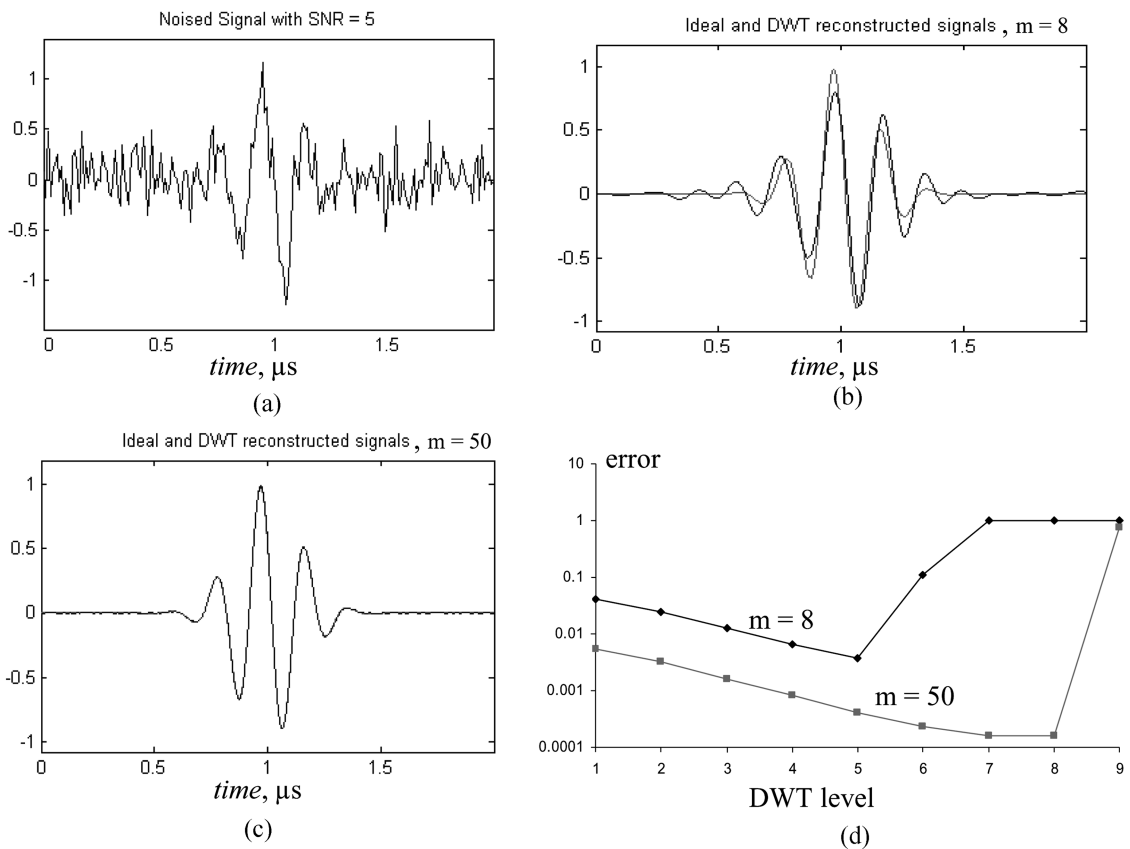


Fig. 5 DWT de-noising: (a) original noised signal with SNR = 5 (Demirli and Sanie 2001); (b) low quality de-noising with  $m = 8$ , level = 1; (c) high quality de-noising with  $m = 50$ , level = 5; (d) variations of error index at different level of  $m = 8$  and  $m = 50$

### 3.2. DWT de-noising

To study the DWT de-noising, the statistical de-noising results achieved by Demirli and Saniie (2001) were used (Fig. 5a). We simulated an ideal wave-packet signal with a 100 MHz sampling frequency over a 2  $\mu$ s duration. Gaussian white noise (GWN) was then added at certain signal to noise ratios (SNR). With DWT de-noising, we found that at high SNR, the DWT worked well and eliminated most of the noises. As SNR decreased, the quality of DWT de-noising also decreased. Meanwhile, DWT cannot completely eliminate the noise in the areas of low signal amplitude.

The DWT de-noising efficiency was found to be affected by two factors: SNR and sampling frequency. The higher the SNR and/or the sampling frequency are, the more efficient the DWT de-noising is. A 2  $\mu$ s signal sampled at 100 MHz results in only 200 data points being recorded, which is rather small for proper analysis. To overcome this, we increased the number of points (and hence the original sampling frequency) by inserting extra points of zero amplitude. The number of points inserted between each pair of original points was  $m$ . Thus, the total number of points was increased from  $N$  to  $N^* = N + m \cdot (N - 1)$ . We call  $m$  the densification factor. Fig. 5 shows the comparisons of signal de-noising with DWT at different levels and with different densification factors.

The original signal had SNR=5. Fig. 5b shows the DWT denoised signal with a densification factor  $m=8$  superposed on the ideal signal. Fig. 5c also shows the DWT-denoised signal with a higher densification factor,  $m=50$ , superposed on the ideal signal. Note that, for the plot in Fig. 5c, the difference between ideal signal and denoised signal is imperceptible. Fig. 5d plots the error index (logarithm scale) for densification of  $m=8$  and  $m=50$ , respectively. Another effect noticed in Fig. 5d is that using a higher densification factor gives a smaller error. It is also observed in Fig. 5d that increasing the DWT level reduces the error in a log-lin manner up to a certain DWT level. However, beyond that, the de-noising process breaks down, and a drastic increase in error is experienced. Thus, a critical DWT level exists at which the de-noising is optimal. The value of this critical DWT level depends on the densification factor,  $m$ .

## 4. Time-frequency analysis by short-time Fourier transform and continuous wavelet transform

All signals collected in EUSR systems are non-stationary, which means the Fourier transform is not applicable. Damage in the structure will change the received reflections and reflections from the damage shows up at a certain instant. The objective of our research is to identify echoes caused by damage. Considering the non-stationary property of signals, time-frequency analysis was used. We generated the time and frequency distribution by using short-time Fourier transform (STFT) and the continuous wavelet transform (CWT). As a modified conventional Fourier transform, STFT has a direct connection to the Fourier transform, making it easy to apply and understand. CWT first was explored as an improvement over STFT, and then was compared to it. In our research, we also used CWT to filter out the frequency component of interest.

STFT gives the time-frequency distribution of the signal by shifting a fixed size window through the signal and taking the Fourier transform of the windowed portions. The windowing of the signal results in trade-offs between the time resolution and the frequency resolution. Wavelet transform have several different forms. The continuous wavelet transform (CWT) is used for time-frequency analysis and will generate the time-frequency representation called scalogram. The discrete wavelet transform (DWT) is

quite different from the CWT and is widely used for time-series analysis and signal de-noising. CWT can give a better time-frequency representation than the short-time Fourier transform since it has the variation in time-frequency resolution.

#### 4.1. Comparison of STFT and CWT

For the STFT analysis, it allows us to select the window type (rectangular, Hanning, Hamming or Kaiser), window size and the step size. The window size is defined as:

$$\text{window size} = \frac{\text{length of input signal}}{\text{usercontrol}} \quad (2)$$

where the *usercontrol* is an integer input by the user to divide the length of the input signal. Step size is how much the window moves forward in terms of data points. It is defined as:

$$\text{step} = \frac{\text{window size}}{\text{usercontrol}} = \frac{\text{length of input signal}}{\text{usercontrol}^2} \quad (3)$$

Fig. 6 presents the results of the STFT analysis using a Hanning window. The signal is collected by PWAS sensor with the 343 kHz excitation frequency. In order to enhance the frequency resolution, the original signal was pre-processed by zero padding. Default value of *usercontrol* is 16. Fig. 6a is the

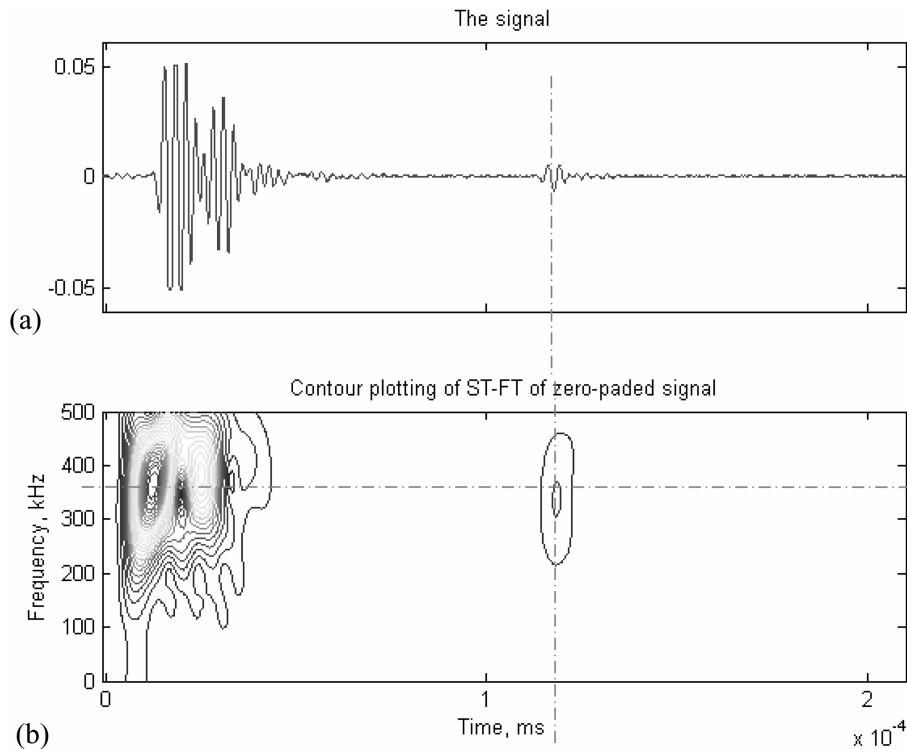


Fig. 6 Short-time Fourier transform analysis: (a) original signal; (b) STFT contour plot

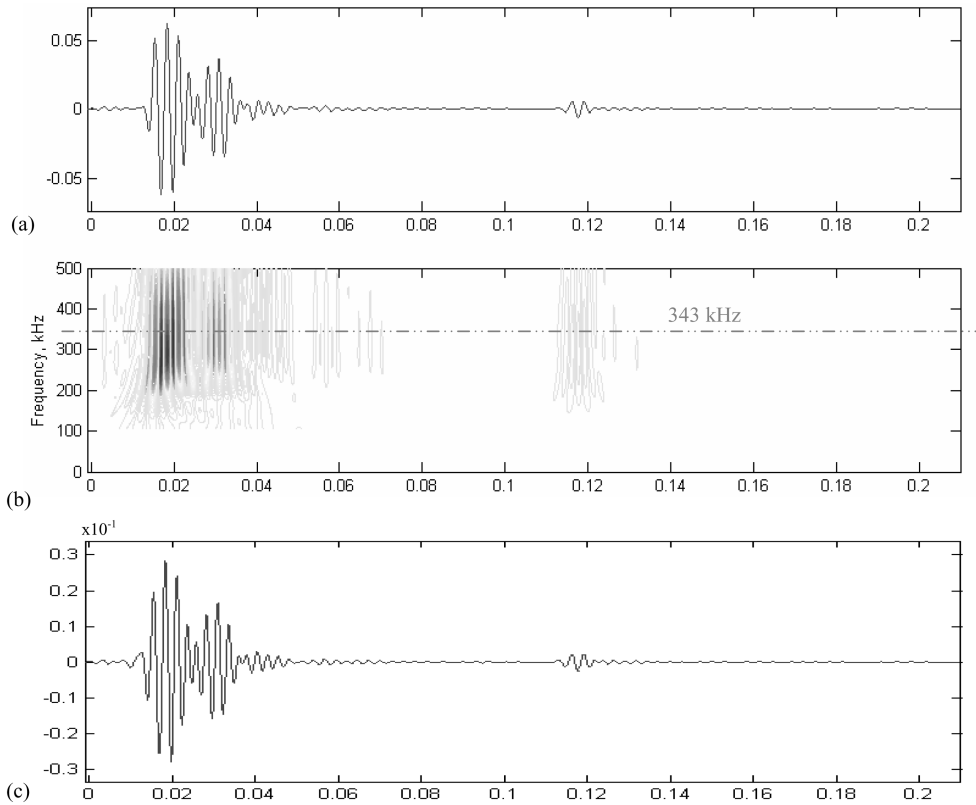


Fig. 7 Continuous wavelet transform on received signal: (a) original signal; (b) CWT spectrum in scale; (c) CWT filtering of the 343 kHz frequency component

original signal, which has two close wave packets with large amplitude. Compared to them, the echo from the crack in the middle is much smaller. Fig. 6b is the STFT spectrogram. The horizontal axis is time axis and the vertical axis is the frequency axis. In this time-frequency plane, the magnitude of each point is represented by contour. Contour is coded that the numerical values are mapped to different closed loops and the density of these loops represents the magnitude of the area. Areas with high density contours have stronger amplitudes and areas with low density contours have weaker amplitudes. It can be found that in the time-frequency plane, the strongest vibration mostly appears at the frequency around 330 kHz and also close to the time when wave packets in Fig. 6a reach their peaks (local maxima). This further confirms that STFT is good representation of non-stationary signal due to its ability to indicate both time and frequency information.

Time-scale/frequency spectra were generated with the CWT method. The user controls included the selection of the mother wavelet, the scale range, and the specific scale of interest. An example of the CWT analysis performing on the signal received by sensor #8 when sensor #1 is triggered is shown in Fig. 7. The time-frequency coordinates provide a more conventional way of interpreting the data. It shows that most of the energy of our signal is concentrated on the frequency of around 340 kHz. Also, the small echo at time about 0.13 ms is observed at scale of 23, which corresponds to a frequency around 340 kHz.

Hence, we see the common characteristics of STFT and CWT are that both give two-dimensional

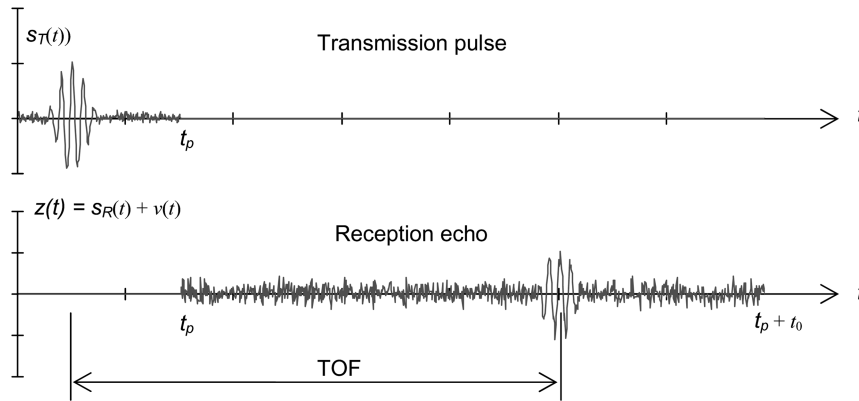


Fig. 8 The basis of pulse-echo method: (a) transmitted smooth-windowed tone-burst of duration  $t_p$ ; (b) received signal to be analyzed for the duration  $t_0$ , starting at  $t_p$ , in order to identify the time of flight

spectra for time-frequency analysis. Yet, they are different in several aspects. The basic difference is that wavelets use a size-adjustable window more advantageous than the fixed window used by STFT (recall that STFT processes the signal with a sliding window having constant length in time). In CWT, the window is variable. At the local area where the signal has a high frequency, e.g., first wave packet in Fig. 6a, the window will be shorter, while where it has a low frequency, e.g., the small echo in the middle of Fig. 6a, the window will be longer. In contrast, STFT cannot get the best results for signals having large frequency changes. In CWT, the window length is adjusted automatically by the CWT algorithm according to the local frequency scale. Also, CWT can easily extract the coefficients at a certain scale that approximately corresponds to the frequency of interest. This is useful for monitoring frequency components that are important for assessing the structural state.

## 5. Signal processing for time-of-flight extraction

As shown in Eq. (4), if we can determine the time of flight TOF of the received waves, we can estimate the location of the reflector from the PWAS array. In this part, we will discuss how to determine TOF by using cross-correlation and Hilbert transform methods.

### 5.1. TOF detection with the raw data

Fig. 9 is the plots of detecting the TOF of the raw data, the signal collected on sensor 1 when sensor 9 is used as the transmitter. Here the ideal excitation 3 counts tone-burst is used as the baseline, as shown in Fig. 9a. Fig. 9c is the envelope of the cross-correlation coefficients. There are a lot of peaks including the one reflecting the TOF of the echo from the crack.

### 5.2. Improved TOF detection by CWT filtering

A typical signal considered in our study is shown in Fig. 8. It consists of a transmission pulse and a reception echo. The reception echo is contaminated with noise. The purpose of our research

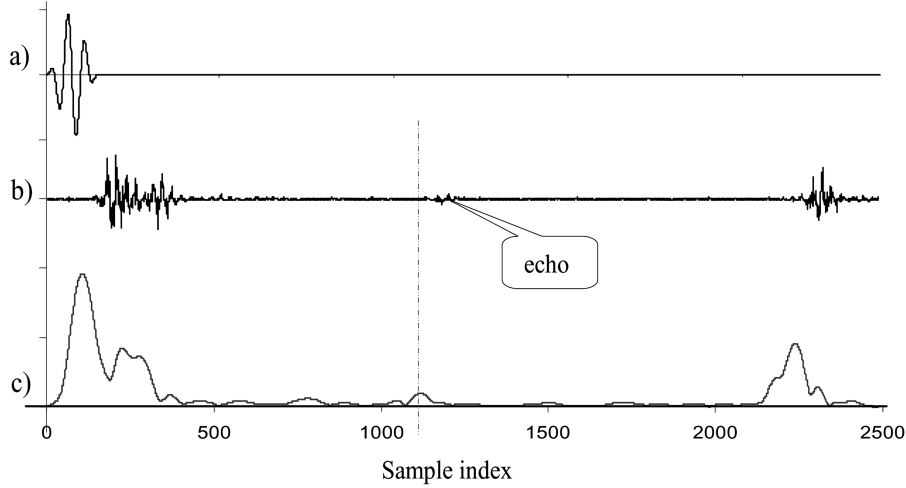


Fig. 9 The result of time-of-flight detection with cross-correlation and Hilbert transform methods: (a) window-smoothed tone-burst baseline; (b) PWAS detected signal; (c) cross-correlation envelope

is to apply advanced signal-processing methods to remove the noise and extract the useful information, such as time of flight (TOF), from the reception signal. If we can find out the TOF, with the given wave propagation speed, the location of the reflector  $d$  can be determined according to the equation:

$$d = v_g \cdot TOF \quad (4)$$

where  $v_g$  is the group velocity of the wave. The difficulty consists in the fact that the signals transmitted and received with the PWAS transducers are much weaker than the signals typically encountered in conventional ultrasonics. This makes the signal processing more challenging and demanding.

From the results showing in Fig. 9, we expect to see better results if we apply certain advanced signal processing methods. Theoretically, signal processing is important in the process of extracting the time-of-flight information from the experimental data. The first step is noise reduction by discrete wavelet transform since the PWAS is very sensitive to vibrations and therefore noise is inevitable, especially when they are used in the field. Once noise is removed, the wave packages are very clear. Time of flight (TOF), signal amplitude and other important information can be visually recognized and ready for further analysis.

### 5.2.1. CWT filtering

From previous Fig. 7b, we can find out our excitation frequency 343 kHz component in the spectrogram since it has most clear magnitude. The disturbance from the background noise was mainly removed by selecting proper contour plot level, which also helped highlight the echo from the damage. Considering that the component of excitation frequency is our major concern (harmonics without dispersive effect), we extracted this single component by using continuous wavelet transform, showing in Fig. 7c.

After we filtered out the 343 kHz component from the received signal, we applied the TOF extraction to it since this component may contain most significant information reflecting the excitation tone-burst, i.e., it may best match the baseline. Fig. 10 shows the results of the whole 343 kHz component.

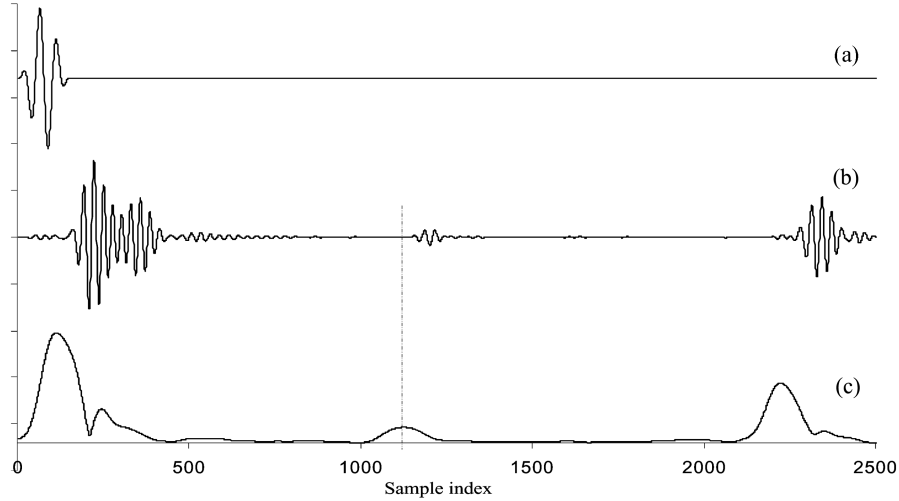


Fig. 10 Cross-correlation of the extracted 343 kHz component: (a) window-smoothed tone-burst baseline; (b) the extracted 343 kHz component; (c) cross-correlation envelope

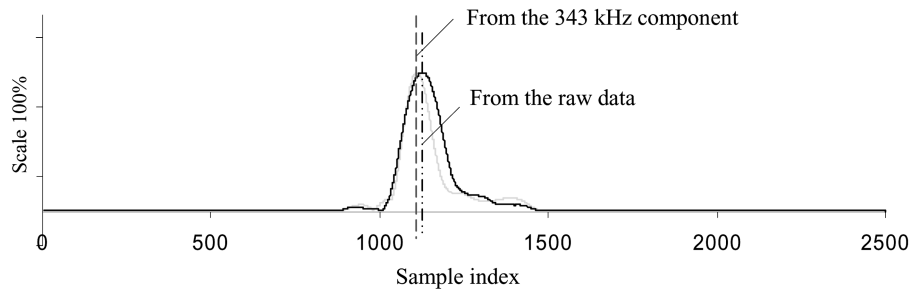


Fig. 11 Comparison of cross-correlation analysis results between raw data and extracted component: (a) tone-burst baseline; (b) the extracted echoes from the raw data and 343 kHz component, respectively; (c) cross-correlation results of raw echo and echo of 343 kHz, respectively

### 5.2.2. Normalization

To compare the results of cross-correlation TOF detection method for echoes extracted from raw data and the single frequency component, we normalized the data by dividing data by the maximum value to make the data fall within 0-1. For better comparison, we cut out the middle wave corresponding to the echo from the crack. The comparison is shown in Fig. 11. From it we can see, the echo from the 343 kHz component looks more like the excitation tone-burst, but it has smaller magnitude than the echo from the raw data since we have removed a part of the embedded noise and the remained 343 kHz component is only a part of the raw data as well. Also we can find that the main frequency component of the echo is 343 kHz. The cross-correlation results further show that that achieved from the 343 kHz has higher precision. Also the peak of the 343 kHz is sharper, which is important for peak detection.

In our proof-of-concept experiments, the tone-burst excitation frequency at 343 kHz ( $S_0$  mode) has the corresponding wave speed  $c = 5440$  mm/s, and the simulated crack on this specimen is 305-mm from the PWAS array at  $\phi_0 = 90^\circ$  degrees. Therefore, according to Eq. (4), and considering the wave needs to travel to and from the crack, we can calculate the theoretical traveling time from the PWAS

Table 1 Data comparison between raw data and 343 kHz component

	Measuring TOF ( $\mu\text{s}$ )	Error (%)	
Result from raw data	114.4	2.03%	Theoretical TOF: 112.12 $\mu\text{s}$
Result from 343 kHz component	112.9	0.7%	

array to the crack and back to the array is:

$$t = 2\tau = 2 \cdot \frac{R}{c} = 2 \cdot \frac{305}{5440} \cdot 10^6 = 112.12 \mu\text{s}$$

Recall our experimental TOF from raw data and 343 kHz component, we have located the peaks at  $N_{raw} = 1144$  and  $N_{343 \text{ kHz}} = 1129$  in terms of data index, respectively. Since the sampling frequency is 10 MHz, therefore transforming to the time from the data index resulted in:  $t_{raw} = 1144 \cdot 0.1 = 114.4 \mu\text{s}$  and  $t_{343 \text{ kHz}} = 1129 \cdot 0.1 = 112.9 \mu\text{s}$ . The error percentage therefore are  $\varepsilon_{raw} = 2.034\%$  and  $\varepsilon_{343 \text{ kHz}} = 0.696\%$ . Fig. 11 indicates the peak locations of the two echoes. Obviously, we have a better TOF detection from the 343 kHz component extracted by CWT filtering.

These showed that the cross-correlation method can accurately detect the arrival time of the wave packet as long as low dispersion is present. This was affirmed by applying CWT filtering. We applied this method with good results in detecting echoes from a small crack in a large plate with 0.7% accuracy.

## 6. Signal processing implementation in the EUSR algorithm

A LabVIEW computer program was developed to control the digital signal collection and recording, construct the inspection data, analyze and process data with advanced signal processing approaches, and image the results for display.

### 6.1. Hilbert transform for envelope extraction

The envelope of a family of curves or surfaces is a curve or surface that is tangent to every member of the family. Envelope extracts the amplitude of a periodic signal. It can be used to simplify the process of detecting the time of arrival for the wave packets in our EUSR system. In the EUSR, the envelope of the signal is extracted by applying Hilbert transform to the cross correlation signal.

The Hilbert transform is defined as:

$$H(x(t)) = -\frac{1}{\pi} \int_{-\infty}^{+\infty} \frac{x(\tau)}{t - \tau} d\tau \tag{5}$$

It can also be defined in terms of convolution theory:

$$H(x(t)) = x(t) * \frac{1}{\pi t} \tag{6}$$

Hilbert transform is often used to construct a complex signal:

$$\tilde{x}(t) = \tilde{x}_{Re}(t) + i \cdot \tilde{x}_{Im}(t) \quad (7)$$

where

$$\begin{aligned} \tilde{x}_{Re}(t) &= x(t) \\ \tilde{x}_{Im}(t) &= H(x(t)) \end{aligned} \quad (8)$$

The real part of the constructed signal,  $\tilde{x}_{Re}(t)$ , is the original data  $x(t)$ , while the imaginary part  $\tilde{x}_{Im}(t)$  is the Hilbert transform of  $x(t)$ . Considering the convolution theory, the Hilbert transform (imaginary part) is a version of the original signal (real part)  $x(t)$  after a  $90^\circ$  phase shift.

Suppose we have a harmonic signal  $u_c(t) = A\cos(2\pi f_c t + \phi_0)$ ,  $f_c$  is the carrying frequency and  $\phi_0$  is the initial phase. We will have the Hilbert transform according to the Hilbert transform property that  $H(\cos(\omega t)) = \sin(\omega t)$ :

$$H(u_c(t)) = A\sin(2\pi f_c t + \phi_0) = A\cos\left(2\pi f_c t + \phi_0 - \frac{\pi}{2}\right) \quad (9)$$

Thus, the Hilbert transformed signal has the same amplitude and frequency content as the original real signal and includes phase information that depends on the phase of the original signal. The magnitude of the complex  $\tilde{x}(t)$  is the same as the magnitude of the origin signal. Therefore, we can say that the magnitude of the analytical signal  $\tilde{x}(t)$  is the envelope of the original signal. Just by observing the envelope signal, the wave packages can be easily recognized.

One aspect of Hilbert transform for envelope detection is, the result may differ from the theoretical envelope if the frequency composition is relatively complicated. For example, we have two simple signals showing in Fig. 12a. The 3 counts tone burst has a carry frequency of 300 kHz and the sinusoid has a frequency of 30 kHz. The synthetic signal indicated in Fig. 12b is constructed simply by adding the two. We see the envelope is far from the smooth envelope we expect to see.

This can be verified analytically with two properties of Hilbert transform:

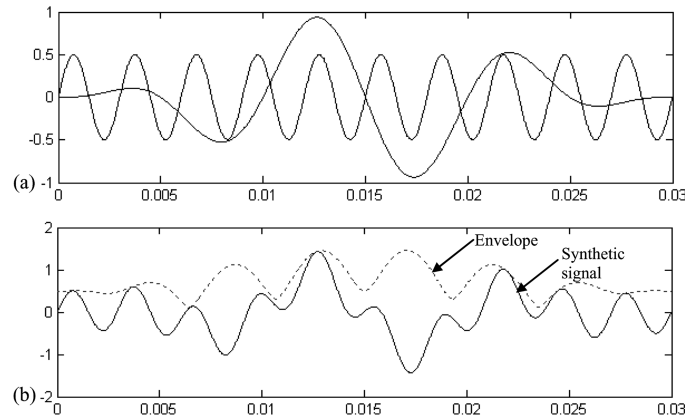


Fig. 12 Hilbert transform example: (a) original signals: black - sinusoid of frequency 30 kHz, blue - 3 counts tone-burst of 300 kHz; (b) the synthetic signal and its envelope extracted by Hilbert transform

1. The often used Hilbert transform pair:  $H(A\cos\varphi) = A\sin(\varphi)$

2. Hilbert transform linearity property:  $H(x(t) + y(t)) = H(x(t)) + H(y(t))$

Assume we have a signal consisting of two frequency components:  $u(t) = A_1\cos\varphi_1 + A_2\cos\varphi_2$ , where  $\varphi_1 = \varphi_1(t)$  and  $\varphi_2 = \varphi_2(t)$ .

The Hilbert transform of  $u(t)$  and the constructing analytical signal  $\tilde{u}(t)$  are:

$$H\{u(t)\} = A_1\sin\varphi_1 + A_2\sin\varphi_2 \quad (10)$$

$$\tilde{u}(t) = A_1\cos\varphi_1 + A_2\cos\varphi_2 + j(A_1\sin\varphi_1 + A_2\sin\varphi_2) \quad (11)$$

To get the amplitudes  $|u(t)|$  and  $|\tilde{u}(t)|$ , here are several conditions to consider:

① If  $\varphi_1 = \varphi_2$ . This means we actually have a single frequency composition. We have  $|u(t)| = A_1 + A_2$  and  $|\tilde{u}(t)| = \sqrt{A_1^2 + A_2^2 + 2A_1A_2} = A_1 + A_2$ . Therefore,  $|u(t)|$  and  $|\tilde{u}(t)|$ , it is verified.

②  $\varphi_1 \neq \varphi_2$  but  $A_1 = A_2$ .

Now  $u(t) = A \cdot 2\cos\left(\frac{\varphi_1 + \varphi_2}{2}\right)\cos\left(\frac{\varphi_1 - \varphi_2}{2}\right)$  and the amplitude  $|u(t)| = 2A$ . The amplitude of  $\tilde{u}(t)$  is:

$$\begin{aligned} |\tilde{u}(t)| &= A\sqrt{(\cos\varphi_1 + \cos\varphi_2)^2 + (\sin\varphi_1 + \sin\varphi_2)^2} \\ &= A\sqrt{\left(2\cos\left(\frac{\varphi_1 + \varphi_2}{2}\right)\cos\left(\frac{\varphi_1 - \varphi_2}{2}\right)\right)^2 + \left(2\sin\left(\frac{\varphi_1 + \varphi_2}{2}\right)\cos\left(\frac{\varphi_1 - \varphi_2}{2}\right)\right)^2} \\ &= 2A\sqrt{\left(\cos^2\left(\frac{\varphi_1 + \varphi_2}{2}\right) + \sin^2\left(\frac{\varphi_1 + \varphi_2}{2}\right)\right)\cos^2\left(\frac{\varphi_1 - \varphi_2}{2}\right)} \\ &= 2A \cdot \left|\cos\left(\frac{\varphi_1 + \varphi_2}{2}\right)\right| \end{aligned}$$

If  $\left|\cos\left(\frac{\varphi_1 + \varphi_2}{2}\right)\right| = 1$ ,  $|u(t)| = |\tilde{u}(t)|$ ; otherwise  $|u(t)| \neq |\tilde{u}(t)|$ .

③  $\varphi_1 \neq \varphi_2$  and  $A_1 \neq A_2$ ,  $|u(t)| = |A_1\cos\varphi_1 + A_2\cos\varphi_2|$

$$\begin{aligned} |\tilde{u}(t)| &= \sqrt{(A_1\cos\varphi_1 + A_2\cos\varphi_2)^2 + (A_1\sin\varphi_1 + A_2\sin\varphi_2)^2} \\ &= \sqrt{A_1^2\cos^2\varphi_1 + A_2^2\cos^2\varphi_2 + 2A_1A_2\cos\varphi_1\cos\varphi_2 + A_1^2\sin^2\varphi_1 + A_2^2\sin^2\varphi_2 + 2A_1A_2\sin\varphi_1\sin\varphi_2} \\ &= \sqrt{A_1^2 + A_2^2 + 2A_1A_2(\cos\varphi_1\cos\varphi_2 + \sin\varphi_1\sin\varphi_2)} \\ &= \sqrt{A_1^2 + A_2^2 + 2A_1A_2\cos(\varphi_1 - \varphi_2)} \end{aligned}$$

For this case, it is difficult to tell  $|u(t)| = |\tilde{u}(t)|$  or  $|u(t)| \neq |\tilde{u}(t)|$  directly, but there are some conditions that  $|u(t)| \neq |\tilde{u}(t)|$ , e.g., when,  $\varphi_1 = 90^\circ$ ,  $\varphi_2 = 0^\circ$ ,  $|u(t)| = |A_2|$ ,  $|\tilde{u}(t)| = \sqrt{A_1^2 + A_2^2}$ . Clearly we can see that  $|u(t)| \neq |\tilde{u}(t)|$ . So we can conclude that  $u(t)$  does not always equal to  $\tilde{u}(t)$ .

Hence, we can conclude, when the signal contains more than one frequency components, the Hilbert

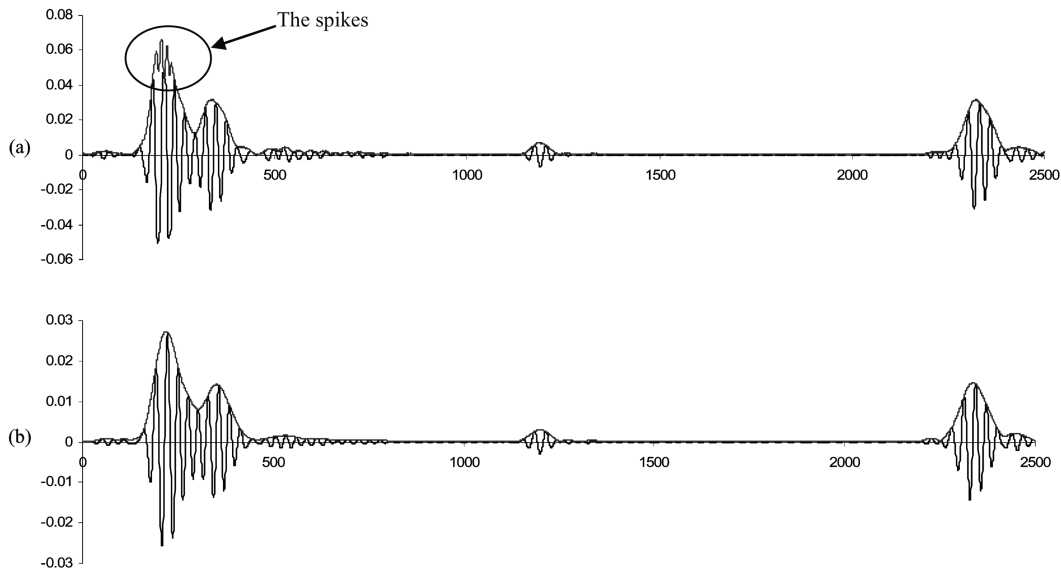


Fig. 13 Hilbert transform for envelope extraction comparison: (a) Hilbert transform for envelope extraction on original received signal; (b) Hilbert transform for envelope extraction on CWT filtered signal

transform for envelope extraction may cause aliasing effect.

In our research, Hilbert transform was used to extract the envelope of a curve. We found out for certain cases Hilbert transform can not extract the right envelope, e.g., shown in Fig. 13a, the first wave packet. Though a single frequency was actually excited in the transmission signal, the receiving back echo always has complicated frequency composition due to dispersion attribute of guided waves and added measurement noise. To extract only the component of excitation frequency, CWT filtering was applied to the wave in Fig. 13a for extracting the component with excitation frequency, 343 kHz and thereafter, Hilbert transform was implemented.

In Fig. 13b we see the spikes showing up in the first packet of Fig. 13a disappeared and we got a smooth envelope of this single frequency component. We experimentally verified and concluded that Hilbert transform works perfectly for extracting the envelope of non-dispersive guided waves with simple frequency composition.

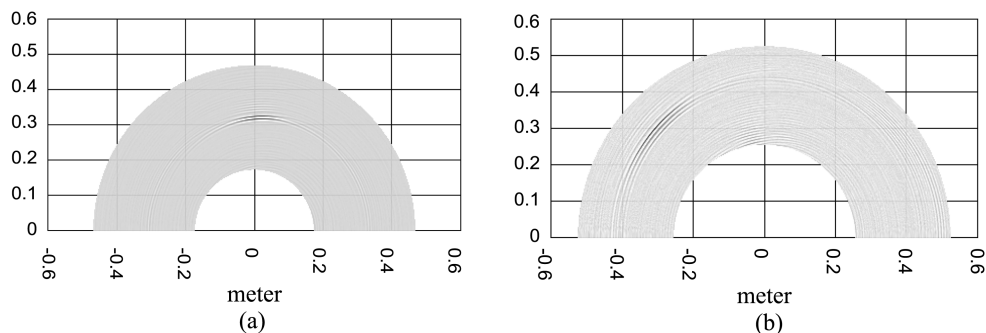


Fig. 14 EUSR inspection images of broadside and offside cracks: broadside crack inspection image; offside crack inspection image

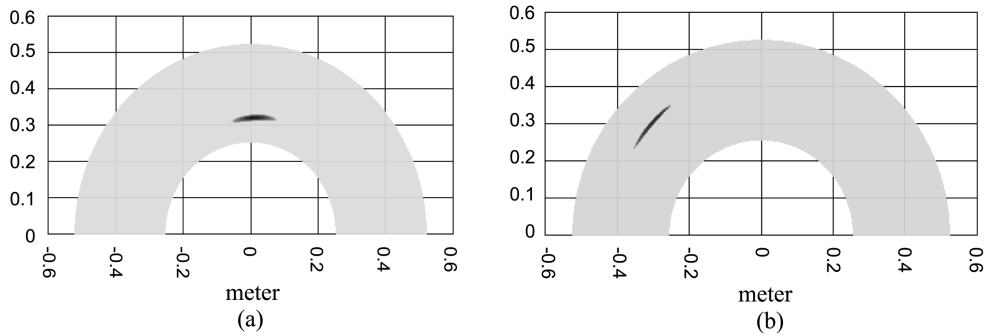


Fig. 15 EUSR inspection images of broadside and offside cracks with using Hilbert transform: (a) broadside crack inspection image; (b) offside crack inspection image

### 6.2. Improved EUSR by Hilbert transform

We have done previous proof-of-concept work by using EUSR to verify its ability for detecting a single crack at either broadside or offside position on a thin-plate specimen, showing in Fig. 14a and b. They are the 2D display of single crack inspection. The offside position is angle  $137^\circ$ .

From these plots, we can see that though they can generally locate the damage, they are far than close to the real cracks. We expected to find a solution to improve the image quality and precision. One thing having been noticed is, the echoes from the damage do not have single peaks due to the dispersion property or some other reasons. Therefore, we need to find a way to make the echoes close to the theoretical ones, i.e., to have single peaks. The method being chosen was the Hilbert transform since it is able to extract the envelope of a curve as we discussed in previous session. An additional thresholding technique was applied as well which is user-controlled. By thresholding, noise whose amplitude is below certain criteria was forced out and the interference was eliminated.

Fig. 15 presents the inspection images with Hilbert transform to extract the envelopes of the echoes. The crack detection shows better resolution and more close to the crack real size. It also has fewer disturbances from the side-lobe effects.

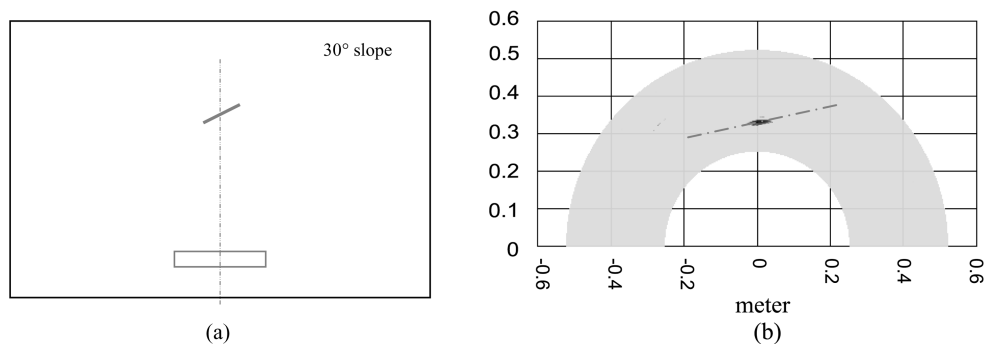


Fig. 16 The broadside crack having  $30^\circ$  slope: (a) schematic; (b) EUSR ‘GUI mapped image

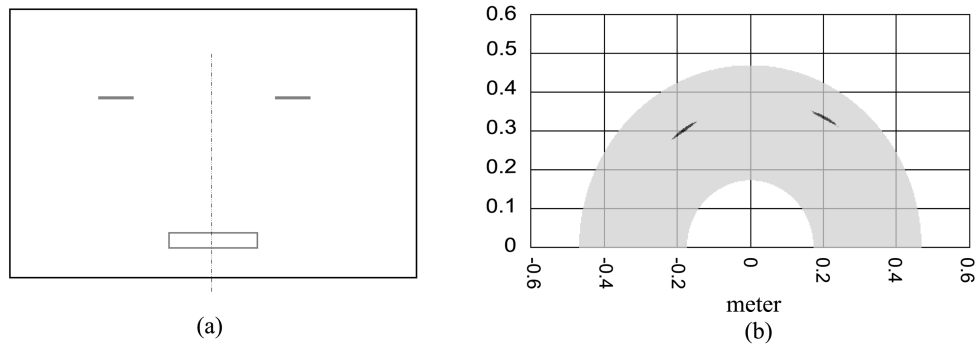


Fig. 17 The two symmetrical offside cracks at  $63^\circ$  and  $137^\circ$ , respectively: (a) schematic; (b) EUSR GUI mapped image

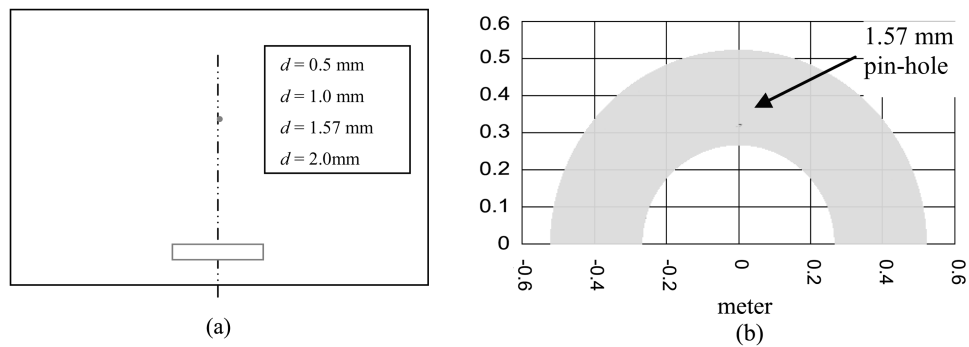


Fig. 18 Pin-holes: (a) schematic; (b) EUSR GUI mapped image of the minimum detectable pin-hole with 1.57 mm diameter

### 6.3. Implementation results

The new experiments are designed to verify the improved EUSR is able to detect complicated cracks and pin-holes as well. Fig. 16 shows the specimen #7 which has a broadside crack with  $30^\circ$  slope to the horizontal. Fig. 16b is the EUSR inspection image. It closely indicates the slope. In the future, we will do further experimentation to find out the minimum slope that EUSR is sensitive and able to indicate.

Our specimen #6, Fig. 17a, has two symmetrical offside cracks at  $63^\circ$  and  $117^\circ$  positions, respectively.

Fig. 17b is the resulting inspection image. One thing has to be mentioned is, for some reason, the two cracks are actually not exactly symmetrical to each other as the original design. They are 3 mm from each vertically. However, the 2D inspection plot picked out such a difference, and we can see the two cracks are in different circles (having different vertical distance to the PWAS array). Therefore we verified that EUSR is able to even pick up that small difference.

Another type of through-plate damage, pin-hole damage was experimented as well. See Fig. 18a. We want to verify EUSR ability to detect these small holes and find out the minimum detectable pin-hole size. The experiment went through hole diameters of 0.5 mm, 1 mm, 1.57 mm and 2 mm. EUSR started detecting the pin hole with 1.57 mm diameter, b. The tiny dot at the broadside position is the simulation of the pin hole in the 2D plot.

## 7. Conclusions

This paper has presented our research work on applying advanced signal processing techniques for using the PWAS EUSR system in structural health monitoring. Embedded PWAS can simultaneously act as transmitters and receivers for sending and receiving Lamb waves in thin-wall structures. The sensors are considered “embedded” into the structure since they are permanently attached to the structure. EUSR has been developed based on the phased array principles with the parallel ray assumption. Several signal processing techniques including de-noising using digital filters and DWT, time-frequency spectrum analysis using STFT and CWT, TOF extraction using cross-correlation, envelope extraction using Hilbert transform, and CWT filtering has also been presented in this paper. The experimental investigation has verified that with the signal processing, the detection ability of EUSR has been improved obviously and can offer more diagnostic information for structural monitoring. We concluded with achieving several interesting points:

1. De-noising process is necessary for removing disturbance from the collected data. We initiate the densification factor for a better de-noising process for using the discrete wavelet transform.
2. Both STFT and CWT analysis can offer useful time-frequency spectrum, while CWT can further be used for single frequency component filtering. Using CWT filtering, we are able to extract the excitation frequency component from the received signal which gives better wave shapes and better envelope extraction when using Hilbert transform.
3. We have verified that Hilbert transform for envelope extraction is precise for signals having single frequency component. When more than one frequencies present, the results will have aliasing. We therefore proposed using the CWT filtering to extract only the frequency component that corresponds to the excitation signal frequency.
4. Cross correlation method combined with Hilbert transform has been used for TOF detection. We have achieved improved TOF by using CWT filtering method to pre-process the signals.
5. The laboratory EUSR experiments so far were successful. It has been verified experimentally that EUSR is able to detect single crack, crack pair, and pin hole defects. With advanced signal processing, image quality has been improved obviously.

One thing needs to note is, as discussed in appendix I, the EUSR algorithm assumes that  $d \ll r$ , i.e., the wave paths from each sensor to the target  $P$  are parallel. Hence for areas close to the phased array, the directional beamforming will be affected and the damage may not be able to be detected. There is a “blind area” around the phased array. In the next step, we will upgrade the parallel algorithm without using the parallel assumption and qualify the blind area of the PWAS phased array. We also plan to implement EUSR inspection to different types of defects and specimens with small size and/or complicated geometry. We will study the beamforming using the guided wave propagation and explore how the beamforming will be affected.

## References

- Acellent ACCESS data management software, Acellent technologies, Inc., <http://www.acellent.com/>.
- Al-khalidy, A., Noori, M., Hou, Z., Yamamoto, S., Masuda, A. and Sone, A. (1997), “Health monitoring systems of linear structures using wavelet analysis”, *International Workshop on Structural Health Monitoring*; 164-75.
- Al-khalidy, A., Noori, M., Hou, Z., Carmona, R., Yamamoto, S., Masuda, A., et al. (1997), “A study of health monitoring systems of linear structures using wavelet analysis”, *ASME PVP*, **347**, 49-58.
- Amaravadi, V., Rao, V., Koval, L.R. and Derriso, M. (2001), “Structural health monitoring using wavelet transforms”,

- Smart Structures and Integrated Systems. Proceedings of SPIE*, **4327**, 258-69.
- Boggess, A. and Narcowich, F. (2001), *A First Course in Wavelets with Fourier Analysis*, Prentice-Hall, Upper Saddle River, NJ 07458.
- Chan, Y. T. (1996), *Wavelet Basics*, Kluwer Academic Publishers, Norwell, MA 02061.
- Cohen, L. (1995), *Time-Frequency Analysis*, Prentice Hall PTR, Englewood Cliffs, NJ 07632.
- Demirli, R. and Saniie, J., (2001), "Model-based estimation of ultrasonic echoes. Part I: analysis and algorithms", *IEEE transaction Ultrasonics, Ferroelectrics, Frequency control*, **48**, 787-802.
- Diaz Valdez, S. H. and Soutis, C. (2000), "Health monitoring of composites using lamb waves generated by piezoelectric devices", *Plastics, Rubber and Composites*, **29**(9).
- Du, W. X., Thurber, C. H. and Phillips, D. E. (2004), "Earthquake relocation using cross-correlation time delay estimates verified with the bispectrum method", *Bulletin of the Seismological Society of America*, **94**(3).
- Elliott, D. (1987), *Handbook of Digital Signal Processing: Engineering Applications*, Academic Press Inc.
- Farrar, C. R., Sohn, H., Fugate, M. L. and Czarniecki, J. J. (2001), "Integrated structural health monitoring", *Proceeding of SPIE Conference on Advanced Nondestructive Evaluation for Structural and Biological Health Monitoring*, March 6-8, 2001, Newport Beach, CA. **4335**, 1-8.
- Forbes, E. and Schaik, A. V. (2000), "Fourier transform and wavelet transform for the time-frequency analysis of bat echolocation signals", <http://www.eelab.usyd.edu.au/andre/reports/batcall.pdf>.
- Giurgiutiu, V. (2003), "Lamb wave generation with piezoelectric wafer active sensors for structural health monitoring", *Proceedings of SPIE's 10th Annual International Symposium on Smart Structures and Materials and 8th Annual International Symposium on NDE for Health Monitoring and Diagnostics*, San Diego, CA.
- Giurgiutiu, V. and Bao, J. (2002), "Embedded ultrasonic structural radar for the nondestructive evaluation of thin-wall structures", *Proceedings of the 2002 ASME International Mechanical Engineering Congress*, New Orleans, LA, paper # IMECE2002-39017.
- Giurgiutiu, V. and Yu, L. (2004), "Advanced signal processing techniques for multi-damage detection with an improved embedded ultrasonic structural radar algorithm and piezoelectric wafer active sensors", *Proceedings of the 2004 ASME International Mechanical Engineering Congress*, Anaheim, CA, paper # IMECE2004-60969.
- Giurgiutiu, V., Blackshire, J. L., Thomas, D. T., Welter, J. T. and Yu, L. (2004), "Recent advances in the use of piezoelectric wafer active sensors for structural health monitoring", *Proceedings of 2<sup>nd</sup> European Workshop on Structural Health Monitoring*, Munich, Germany, 1083-1090.
- Giurgiutiu, V., Yu, L. and Thomas, D. (2004), "Embedded ultrasonic structural radar with piezoelectric wafer active sensors for damage detection in cylindrical shell structures", *Proceedings of 45<sup>th</sup> AIAA/ASME/ASCE/AHS/ASC Structures, Structural Dynamics & Materials Conference and 12<sup>th</sup> AIAA/ASME/AHS Adaptive Structures Forum*, Palm Springs, CA, paper # AIAA-2004-1983.
- Giurgiutiu, V. and Yu, L. (2003), "Comparison of short-time fourier transform and wavelet transform of transient and tone burst wave propagation signals for structural health monitoring", *Proceedings of 4<sup>th</sup> International Workshop on Structural Health Monitoring*, Stanford, CA, 1267-1274.
- Graps, A. An Introduction to Wavelets, IEEE computational Science and Engineering, Summer 1995, Vol. 2, No. 2, published by IEEE Computer Society, 10662 Los Vaqueros Circle, Los Alamitos, CA 90720
- Handzel, A. A., Anderson, S. B., Gebremichael, M. and Krishnaprasad, P. S. (2003), "A biomimetic apparatus for sound-source localization", *Processing of the 42<sup>nd</sup> IEEE Conference on Decision and Control*, Maui, Hawaii, USA.
- Hans, S., Ibraim, E., Pernot, S., Boutin, C. and Lamarque, C. H. A. (2000), "Damping identification in multi-degree-of-freedom systems via a wavelet-logarithmic decrement - Part 2: study of a civil engineering building", *J Sound Vib*, **235**(3), 375-403.
- Hou, Z., Noori, M. and Amand, R. S. (2000), "Wavelet-based approach for structural damage detection", *J. Eng. Mech*, **126**(7), 677-683.
- Hou, Z. and Hera, A. (2001), "System identification technique using truncated pseudo wavelet transform", *Proceeding of SPIE 2001 Smart Structures and Materials*, **4326**, 198-267.
- Hu, X., Ji, Y. and Yu, W. (2001), "The application of wavelet singularity detection in fault diagnosis of high voltage breakers", *Processing of the 27<sup>th</sup> Annual Conference of the IEEE Industrial Electronics Society*, Denver, Colorado.
- Hueber, G., Ostermann, T., Bauernfeind, T., Raschhofer, R. and Hagelauer, R. (2000), "New approach of ultrasonic distance measurement technique in robot applications", *Processing of International Conference on Signal*

- Processing, Beijing, China.
- Jiang, Z. and Kabeya, K. (1999), "Longitudinal wave propagation measuring technique for structural health monitoring", *Proceedings of SPIE 1999, Smart Structures and Integrated Systems*, **3668**, 343-350.
- Kang, M. S., Stanbridge, A. B., Chang, T. G. and Kim, H. S. (2000), "Measuring mode shapes with a continuously scanning laser vibrometer - Hilbert transform approach", *J. Mech. Systems and Signal Proc.*, **16**(2-3), 201-210.
- Kay, S. (1998), *Fundamentals of Statistical Signal Processing, Detection Theory*, Prentice Hall PTR, Upper Saddle River, NJ 07458.
- Kim, H. and Melhem, H. (2004), "Damage detection of structures by wavelet analysis", *J. Eng. Struct.*, **26**, 347-362.
- Kitada, Y. (1998), "Identification of nonlinear structural dynamic systems using wavelets", *J. Eng. Mech.*, **124**(10), 1059-1066.
- Knapp, C. H. and Carter, G. C. (1976), "The generalized correlation method for estimation of time delay", *IEEE Transaction of Acoustic, Speech, Signal Processing*, **24**, 320-327.
- Lamarque, C. H. and Pernot, C. (2000), "Damping identification in multidegree-of-freedom systems via a wavelet-logarithmic decrement - Part 1: theory", *J. Sound Vib.*, **235**(3), 361-74.
- Mal, A. (2001) "NDE for health monitoring of aircraft and aerospace structures", *Proceedings of the 7<sup>th</sup> ASME NDE Topical Conference, NDE-Vol. 20*, 149-155.
- Marioli, D., Narduzzi, C., Offelli, C., Petri, D., Sardini, E. and Taroni, A. (2000), "Digital time-of-flight measurement for ultrasonic sensors", *IEEE transaction on Instrumentation and Measurement*, **41**(1).
- Purekar, A. and Pines, D. J. (2003), "Damage interrogation using a phased piezoelectric sensor/actuator array: simulation results on two dimensional isotropic structures", *44<sup>th</sup> AIAA/ASME/ASCE/AHS Structures, Structural Dynamics, and Materials Conference*, Norfolk, VA, paper #AIAA 2003-1565, p1-9.
- Rioul, O. and Vetterli, M. (1991), "Wavelets and signal processing", *IEEE SP magazine*, pp.14-35.
- Robertson, A. N., Park, K. C., Alvin, K. F. (1998), "Extraction of impulse response data via wavelet transform for structural identification", *J. Vib. Acoust.*, **120**, 252-260.
- Ruzzene, M., Fasana, A., Garibaldi, L. and Biombo, B. (1997), "Natural frequencies and dampings identification using wavelet transform: application to real data", *Mech Syst Signal Process*, **11**(2), 207-218.
- Schlaikjer, M., Bagge, J. P., Sorensen, O. M. and Jensen, J. A. (2003), "Trade off study on different envelope detectors for b-mode imaging", *Processings of 2003 IEEE Ultrasonics Symposium*, Hawaii, USA.
- Staszewski, W. J. (2002), "Intelligent signal processing for damage detection in composite materials", *J. Comp. Sci. Tech.*, **62**, 941-950.
- Sundaraman, S. and Adams, D. E. (2002), "Phased transducer arrays for structural diagnostics through beamforming", *17<sup>th</sup> Technical Conference of the American Society for Composites*, West Lafayette, IN, Paper # 177.
- Tong, C. and Figueroa, F. (2001), "A method for short or long range time-of-flight measurements using phase-detection with an analog circuit", *IEEE Transactions on Instrumentation and Measurement*, **50**(5).
- Tsai, D. M., Lin, C. T. and Chen, J. F. (2003), "The evaluation of normalized cross correlation for defect detection", *J. Pattern Recognition Letters*, **24**, 2525-2535.
- Vishay Micro-Measurements Instruction Bulletin B-127-14, *Strain Gauge Installation with M-Bond 200 Adhesive*, Malvern, PA.
- Wimmer, S. A. and Degiorgi, V. (2004), "Detecting damage through the application of a continuous wavelet transformation-based algorithm", *Proceedings of SPIE's 11<sup>th</sup> Annual International Symposium on Smart Structures and Materials and 9<sup>th</sup> Annual International Symposium on NDE for Health Monitoring and Diagnostics*, San Diego, CA, paper #5394-40.
- Yang, J. N., Lin, S., Wang, R. and Zhou, L. (2004), "Identification of parametric changes for structural health monitoring using an adaptive filtering technique", *Proceedings of SPIE's 11<sup>th</sup> Annual International Symposium on Smart Structures and Materials and 9<sup>th</sup> Annual International Symposium on NDE for Health Monitoring and Diagnostics*, San Diego, CA, paper #5391-39.
- Yu, L., Bao, J. and Giurgiutiu, V. (2004), "Signal processing techniques for damage detection with piezoelectric wafer active sensors and embedded ultrasonic structural radar", *SPIE's 11<sup>th</sup> Annual International Symposium on Smart Structures and Materials and 9<sup>th</sup> Annual International Symposium on NDE for Health Monitoring and Diagnostics*, San Diego, CA, paper # 5391-52.

## Appendix I

The principle of operation of the embedded ultrasonic structural radar (EUSR) is derived from two general principles: (1) The principle of guided Lamb wave generation with piezoelectric wafer active sensors (PWAS); (2) The principles of conventional phased-array radar.

The guided Lamb waves generated by PWAS have the important property that they stay confined inside the walls of a thin-wall structure, and hence can travel over large distances. In addition, the guided wave can also travel inside curved walls, which makes them ideal for applications in the ultrasonic inspection of aircraft, missiles, pressure vessel, oil tanks, pipelines, etc. This has been proved by our curvature experiment. Lamb waves can exist in a number of dispersive modes. However, through smoothed tone-burst excitation and frequency tuning, it is possible to confine the excitation to a particular Lamb wave mode, of carrier frequency  $f_c$ , wave speed  $c$ , and wave length  $\lambda = c / f_c$ . Hence, the smoothed tone-burst signal generated by one PWAS is of the form:

$$s_T(t) = s_0(t)\cos 2\pi f_c t \quad (12)$$

where  $s_0(t)$  is a short-duration smoothing window that is applied to the carrier signal of frequency  $f_c$  between 0 and  $t_p$ . The principle of conventional phased-array radar is then applied to the PWAS-generated guided waves, assuming a uniform linear array of  $M$  PWAS, with each PWAS acting as a pointwise omni-directional transmitter and receiver. The PWAS in the array are spaced at the distance  $d$ , which is assumed much smaller than the distance  $r$  to a generic, far-distance point,  $P$ . Since  $d \ll r$ , the rays joining the sensors with the point  $P$  can be assimilated with a parallel fascicle, of  $\phi$ . Therefore, for the  $m^{\text{th}}$  PWAS, the distance will be shorted by  $m(d\cos\phi)$  (a). If all the PWAS are fired simultaneously, the signal from the  $m^{\text{th}}$  PWAS will arrive at  $P$  quicker by  $\Delta_m(\phi) = m(d\cos\phi) / c$ . Yet, if the PWAS are not fired simultaneously, but with some individual delays,  $\delta_m$ ,  $m=0,1,\dots,M-1$ , then the total signal received at point  $P$  will be:

$$s_P(t) = \frac{1}{\sqrt{r}} \sum_{m=0}^{M-1} s_T\left(t - \frac{r}{c} + \Delta_m(\phi) - \delta_m\right) \quad (13)$$

$1/r$  represents the decrease in the wave amplitude due to the omni-directional 2-D radiation, and  $r/c$  is the delay due to the travel distance between the reference PWAS ( $m=0$ ) and the point  $P$ . (Here wave-energy conservation, i.e., no dissipation, is assumed.)

Transmitter beamforming: if we have  $\delta_m = m\Delta(\phi)$ , then Eq. (13) becomes:

$$s_P(t) = M \cdot \frac{1}{\sqrt{r}} s_T\left(t - \frac{r}{c}\right) \quad (14)$$

That's to say, there is an  $M$  times increase in the signal strength with respect to a simple sensor. This leads directly to the beamforming principle that if  $\delta_m = m d \cos(\phi_0) / c$ , and since  $\Delta_m = m d \cos(\phi) / c$ , then constructive interference (beamforming) takes place when  $\cos(\phi) = \cos(\phi_0)$ , i.e., at angles  $\phi = \phi_0$  and  $\phi = -\phi_0$ . Thus, the forming of a beam at angles  $\phi_0$  and  $-\phi_0$  is achieved through delays in the firing of the sensors in the array.

Receiver beamforming: if the point  $P$  is an omni-directional source at azimuth  $\phi_0$ , then the signals received at the  $m^{\text{th}}$  sensor will arrive quicker by  $m\Delta_0\phi = m d \cos(\phi_0) / c$ . Hence, we can synchronize the signals received at all the sensors by delaying them by:

$$\delta_m(\phi_0) = m \frac{d}{c} \cos(\phi_0) \quad (15)$$

**Pulse-echo method:** Assume that a target exists at azimuth  $\phi_0$  and distance  $R$ . The transmitter beamformer is sweeping the range in increasing angles  $\phi$  and receives an echo when  $\phi = \phi_0$ . The echo will be received on all sensors, but the signals will not be synchronized. To synchronize the sensors signals, the delays  $\delta_m(\phi_0) = md\cos(\phi_0)/c$  need to be applied.

The original signal is:

$$s_P(t) = \frac{M}{\sqrt{R}} s_T\left(t - \frac{2R}{c}\right) \quad (16)$$

At the target, the signal is backscattered with a backscatter coefficient  $A$ . Hence, the signal received at each sensor will be:

$$\frac{A \cdot M}{R} s_T\left(t - \frac{2R}{c} + \Delta_m(\phi)\right) \quad (17)$$

The receiver beamformer assembles the signals from all the sensors with the appropriate time delays:

$$s_R(t) = \frac{A \cdot M}{R} \sum_{m=0}^{M-1} s_T\left(t - \frac{2R}{c} + \Delta_m(\phi) - \delta_m\right) \quad (18)$$

Constructive interference between the received signals is achieved when  $\delta_m(\phi_0) = md\cos(\phi_0)/c$ . Thus, the assembled receive signal will be again boosted  $M$  times (Fig. 19b):

$$s_R(t) = \frac{A \cdot M^2}{R} \sum_{m=0}^{M-1} s_T\left(t - \frac{2R}{c}\right) \quad (19)$$

The array response is a function of both time and the orientation angle according to Eqs. (15) and (19). The implementation of EUSR is illustrated in Fig. 2a of the paper. An aluminum plate was instrumented with a number  $M$  of PWAS transducers arranged in a linear phased array. In order to implement the phased array principle, an array of  $M^2$  elemental signals is collected. The  $M^2$  elemental signals are obtained by performing excitation of one PWAS and detection on all the PWAS, in a round robin fashion. After the  $M^2$  signals are collected and stored in the computer memory, the phased array

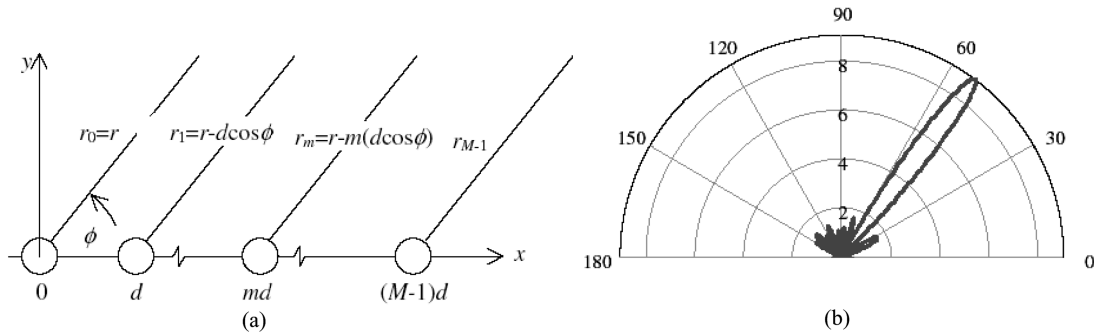


Fig. 19 (a) a phased array spacing at distance  $d$ ; (b) the calculated beamforming pattern for a  $M$  PWAS array with  $\phi = 53^\circ$

principle is applied in virtual time using the EUSR algorithm and the EUSR LabVIEW program described by Giurgiutiu and Bao (2002). The azimuthal angle  $\phi$  is allowed to vary in the range  $0^\circ$  to  $180^\circ$  to attain, a sweep of the complete half plane. At each  $\phi$ , an A-scan of the Lamb wave beam signal is obtained. If the beam encounters damage within the boundary of the plate under inspection, reflection/diffraction from the damage will show as an echo in the A-scan, as shown in Fig. 2b. It indicates clearly the crack echo because the scanning beam is oriented at  $90^\circ$ . Azimuthal juxtaposition of all the A-scan signals creates an image of the half plane. The damage is clearly indicated as darker areas. Using the wave speed value, the time domain signals are mapped into the space domain and the geometric position and a measuring grid is superposed on the reconstructed image. Thus, the exact location of the defects can be directly determined. The angle relative to the greatest array response and the distance to the damage from the array needs to be determined. To determine the distance, the time of flight of echoes needs to be detected first using (Purekar and Pines 2003, Sundaraman and Adams 2002):

$$R = c\tau / 2 \quad (20)$$

Therefore, what we need to determine from the signals is the time delay between the receive signal,  $s_R(t)$  and the transmit signal  $s_T(t)$ . Fig. 8 in the paper shows the transmitted and received signals.

## Appendix II

### A.1. Short-time fourier transform

The short-time Fourier transform is a widely used method for studying non-stationary signals. The concept behind it is simple and powerful. The basic idea of the short-time Fourier transform is to break up the signal into small time segments and do the Fourier analysis on each time segment to confirm that certain frequencies exist or occur in that segment. The totality of the spectra of the segments will indicate how the spectrum varies with time. However we cannot divide the signal into finer and finer part due to the uncertainty principle:

$$\Delta\omega \cdot \Delta t \geq \frac{1}{2} \quad (21)$$

The uncertainty principle states that the product of the standard deviation in time and frequency (time and frequency resolutions) is limited. The decrease (increase) in frequency resolution results in an increase (decrease) in time resolution and vice versa. Further more, if we cut the signal into too small parts, they will lose the connection to the original signal and therefore cannot indicate the original signal's properties.

Suppose we have a signal  $s(t)$ . To study the signal properties at time  $t_0$ , windowing processing is applied to emphasize the signal at that instant and suppress those at other time. The window, indicated by a function  $h(t)$ , is centered at  $t$ . The windowing process will produce a modified signal:

$$S_t(\tau) = s(\tau)h(\tau - t) \quad (22)$$

This modified signal is a function of the fixed time,  $t$ , and the varying time  $\tau$ .

The corresponding Fourier transform of signal  $S_i(\tau)$  is:

$$S_i(\omega) = \frac{1}{2\pi} \int e^{-j\omega\tau} s_i(\tau) d\tau = \frac{1}{2\pi} \int e^{-j\omega\tau} s(\tau) h(\tau-t) d\tau \quad (23)$$

The energy density spectrum at time  $t$  is:

$$P_{SP}(t, \omega) = |S_i(\omega)|^2 = \frac{1}{2\pi} \int e^{-j\omega\tau} s(\tau) h(\tau-t) d\tau|^2 \quad (24)$$

For each different time, we get a different spectrum and the totality of these spectra is the time-frequency distribution  $P_{SP}$ , called spectrogram.

The effects of two key parameters, window length,  $\tau$ , and time interval,  $d\tau$ , between two consecutive windows, were investigated in our research. Contour plot was applied in the spectrogram to represent the amplitude of each point in the time-frequency space. A graphical user interface (GUI) has been developed to control the analyzing procedure for best parameter combination.

## A.2. Continuous wavelet transform

Continuous wavelet transform (CWT) is similar to the STFT, except that instead of a basis of infinite sines and cosines of different frequencies, the CWT compares the signal with dilated and shifted versions of a single basis function called mother wavelet (Graps 1995). The CWT of signal  $s(t)$  by using mother wavelet  $\psi(t)$  is:

$$CWT(a, \tau) = \frac{1}{\sqrt{a}} \int s(t) \psi\left(\frac{t-\tau}{a}\right) dt \quad (25)$$

and

$$\int \psi(t) dt = 0 \quad (26)$$

$a$  is dilation and  $\tau$  is the shift of the wavelet with respect to the signal. If  $\psi(t)$  is considered as the impulse response of a bandpass filter, the CWT can be understood through bandpass analysis. As scale  $a$  increases, the center frequency and the bandwidth of the bandpass filter will increase. The CWT resolutions depend on the scale. At low scale (high frequency), the time resolution is good, but the frequency resolution is bad due to the fact that the wavelet is well localized in time but poorly in frequency. The magnitude squared  $|CWT(a, \tau)|^2$  is defined as the scalogram. Fig. 20 lists several often used wavelets.

A GUI LabVIEW program has been developed to allow us to pick out satisfactory mother wavelets, wavelet analysis levels, and scales. CWT automatically produces a spectrum of time-scale vs. amplitude. Corresponding spectrum of time-frequency vs. amplitude was also generated according to the quasi-relationship between the scale and the corresponding frequency:

$$f = \frac{\text{center frequency of the wavelet}}{\text{scale} \cdot \text{sampling interval}} \quad (27)$$

Considering that a particular frequency may need special attention, the coefficients at a certain scale (frequency) were also generated.

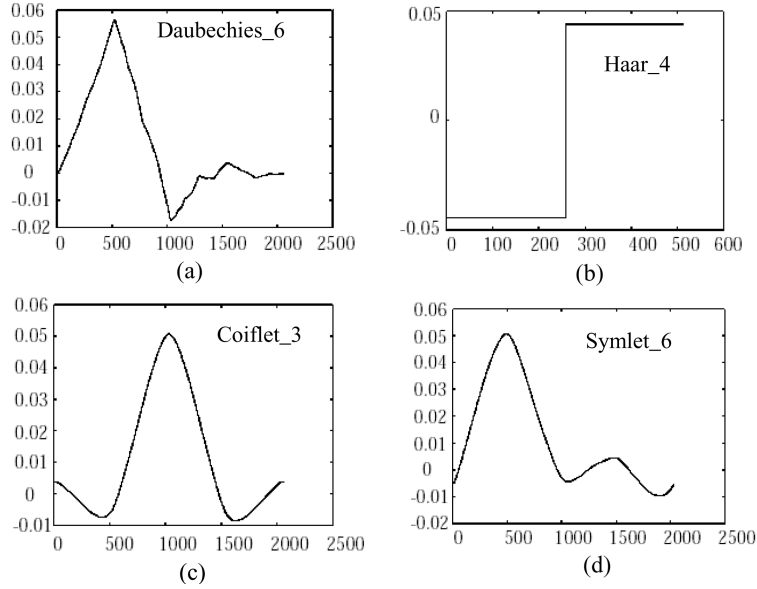


Fig. 20 Several often used wavelets: (a) Daubechies wavelet; (b) Haar wavelet; (c) Coiflet wavelet; (d) Symlet wavelet (Graps 1995)

### A.3. Discrete wavelet transform

In DWT, the dilations and translations of the mother wavelet  $\psi(t)$  define our orthogonal basis, the wavelet basis:

$$\psi_{(s,l)}(t) = 2^{-s/2} \psi(2^{-s}t - l) \quad (28)$$

The variables  $s$  and  $l$  are integers that scale and dilate the mother wavelet  $\psi(t)$  to generate wavelets, such as a Daubechies wavelet family. The scale index  $s$  indicates the wavelet's width, while the location index  $l$  gives its position. To span our data domain at different resolutions, the analyzing wavelet is used in the scaling equation:

$$W(x) = \sum_{k=-1}^{N-2} (-1)^k c_{k+1} \psi(2x+k) \quad (29)$$

where  $W(x)$  is the scaling function for the mother wavelet  $\psi(t)$ , and  $c_k$  are the wavelet coefficients. The wavelet coefficients must satisfy linear and quadratic constraints of the form:

$$\sum_{k=0}^{N-1} c_k = 2, \quad \sum_{k=0}^{N-1} c_k c_m = 2\delta_{m,0} \quad (30)$$

where  $\delta$  is the delta function and  $m$  is the location index.

The coefficients  $\{c_0, \dots, c_n\}$  are usually thought as a filter. These coefficients, or the filter, are placed in a transformation matrix, which is applied to the raw data. The coefficients are ordered using two

dominant patterns, one that works as a smoothing filter (like a moving average), and one pattern that works to bring out the data’s detail information. The coefficient matrix is applied in a hierarchical algorithm. In the matrix, the odd rows contain an ordering of wavelet coefficients that act as the smoothing filter, and the even rows contain an ordering of wavelet coefficients with different signs that act to bring out the data’s detail. The matrix is first applied to the original, full-length vector. Then the vector is smoothed and “decimated” in half and the matrix is applied again. Then the smoothed, halved vector is smoothed and halved again by applying the matrix once more. This process continues until a few data remain which within the user-defined allowable error range. That is, each matrix application brings out a higher resolution of the data while at the same time smoothing the remaining data. The output of the DWT consists of the remaining smooth components and all of the accumulated detail components.

#### A.4. Digital filters

In digital signal processing, filters are often used to remove or to keep certain parts of the signal. Filters are characterized by their frequency responses in the frequency domain. They are categorized into two groups known as Finite-duration Impulse Response (FIR) filters for which the impulse response is non-zero for only a finite number of samples, and Infinite-duration Impulse Response (IIR) for which the impulse response has an infinite number of non-zero samples. IIR filters are also known as the feedback filters since their filter coefficients include feedback terms in a difference equation. Compared to FIR filters, IIR filters can achieve the desired design specifications with a relatively low order so that fewer unknown parameters need to be computed and stored, which might lead to a lower design and implementation complexity. The realizable filter can be found by optimizing some measure of the filter’s performance, e.g., minimizing the IIR filter order, minimizing the width of the transition bands, or reducing the passband and/or stopband error, etc. through controls in the GUI. Equation is the frequency response  $H(\omega)$  of IIR filters.  $N$  is the filter order, which can be considered as a free parameter for optimization. Filter order determines the number of previous output samples that need to be stored and then fed back to compute the current output sample.

$$H(\omega) = \frac{B(\omega)}{A(\omega)} = e^{-j\omega N_0} \frac{\sum_{k=0}^M b_k e^{-j\omega k}}{\sum_{k=0}^M a_k e^{-j\omega k}} \quad (31)$$

The four classical IIR filter types are (1) Butterworth, (2) Chebyshev I, (3) Chebyshev II, (4) Elliptic. Each filter has its own characteristics in terms of performance.

#### A.5. Cross-correlation

Cross correlation is used to detect similarities in two signals. The cross correlation  $R_{xy}(t)$  of two signals  $x(t)$  and  $y(t)$  is defined by

$$R_{xy}(t) = \int_{-\infty}^{+\infty} x(\tau)y(\tau + t)d\tau \quad (32)$$

For discrete-time signals, Eq. (32) can be expressed as:

$$R_{XY}(m) = \frac{1}{N} \sum_{n=0}^{N-1} x(n)y(n - m) \quad (33)$$

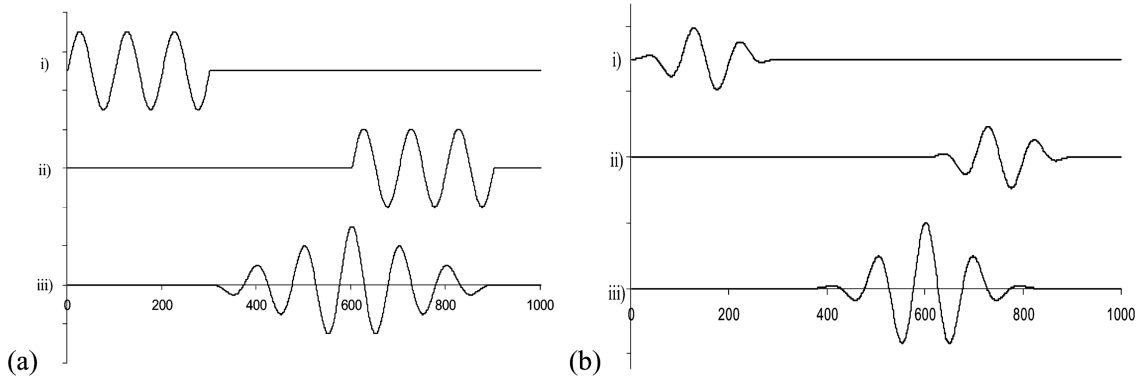


Fig. 21 Cross-correlation of simulated tone-burst signals: (a) 3-count sine signal: (b) 3-count Hanning-window smoothed signal. Note: (i) transmitted signal  $x(t)$ ; (ii) received signal  $y(t)$ ; (iii) cross-correlation of  $x(t)$  and  $y(t)$

To illustrate how the method works, we use a 3-count sinusoidal signal (tone-burst) as an example which is generated at the transmitting active sensor from a sinusoidal signal  $x(t) = \sin(2\pi t)$  with period  $T = 1 \mu\text{s}$  starting at  $t_0 = 0 \mu\text{s}$  and vibrating for 3 cycles. This signal arrives at the receiving sensor at  $t_1 = 600 \mu\text{s}$ . See a. The first signal-*i* is the transmitting signals and the one below it signal-*ii* is the receiving signal. The cross-correlation coefficient  $R_{xy}(t)$  is shown at the bottom as signal-*iii*, with a peak right at  $t_1 = 600 \mu\text{s}$ .

The process of generating the cross correlation coefficients can be explained as followed: the input signal slides along the time axis of the correlated signal with a small step while the similarity of the overlapped part of two signals is compared. Before the tail of the input signal hits it, the two signals are not related and the corresponding cross correlated coefficients is 0. When the input signal arrives at  $t_1 = 600 \mu\text{s}$ , the two signals completely overlap, i.e., they match perfectly. At this moment, the cross correlation coefficient  $R_{xy}(t)$  also reaches the maximum value (see bottom figure in Fig. 21). After the input signal moves away from the best match point  $t_1 = 600 \mu\text{s}$ , the similarity between the overlapped parts becomes smaller again. Also the cross correlation coefficients decrease. When the input signal totally moves away the compared signal, the overlapping is none and the coefficients become zeros.

Fig. 21b illustrates the cross-correlation results of window-smoothed tone-burst signals. Assume the time-of-flight (TOF) of the received signal is still  $t_1 = 600 \mu\text{s}$ . As explained before, the received signal is compared with the transmitted signal by sliding through the time axis. With the transmitted signal moves forward, the resulting coefficients  $R_{xy}(t)$  change from 0 to small values, increasing, and then hitting the peak, and decreasing till become 0 again. From bottom cross-correlation coefficients curve *iii*, we see a peak showing up at  $t_1 = 600 \mu\text{s}$ , which is exactly the arrival time of the received signal.

An extra bonus using the cross correlation method is, for real signals which have unavoidable noise, it can reduce the annoyance of noise since the noise is not related to the signals and not auto-related either. We employed an example signal from the proof-of-concept experiment of the EUSR system collected by PWAS. The excitation signal was a window-smoothed 3-count tone-burst of 343 kHz carry frequency. This signal was used as the baseline signal in the cross-correlation method, shown as Fig 22a. The received signal, shown in Fig. 22b, carried significant noise, which hampered the detection of the time of flight of the echo reflected by the crack. Cross correlation generated the coefficient curve in Fig. 22c. Note that it has several local maxima, corresponding to the arrival time of each wave packet.

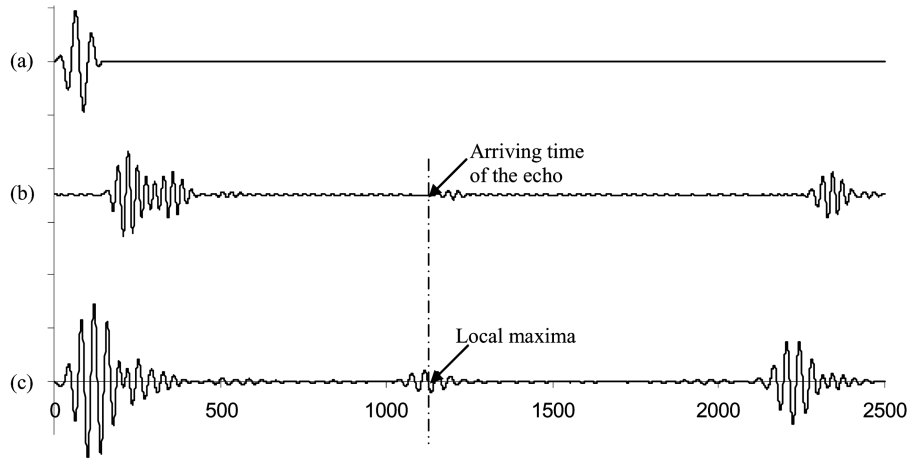


Fig. 22 cross-correlation of PWAS signals: (a) window-smoothed tone-burst as the baseline; (b) PWAS received signal; (c) cross-correlation of the signals

The noise may contaminate the original signal, but it will not significantly affect the cross-correlation result. By applying some peak detection method, we can pick out those peaks and therefore, determine the arrival time of each wave packets.

CC